The retrieval of snow properties from SLSTR/ Sentinel-3 - part 1: method description and sensitivity study

Linlu Mei[1], Vladimir Rozanov[1], Christine Pohl[1], Marco Vountas[1], John P. Burrows[1]

[1] Institute of Environmental Physics, University of Bremen, Germany

Abstract

The eXtensible Bremen Aerosol/cloud and surfacE parameters Retrieval (XBAER) algorithm has been designed for the Top-Of-Atmosphere reflectance measured by the Sea and Land Surface Temperature Radiometer (SLSTR) instrument onboard Sentinel-3 to derive snow properties: Snow Grain Size (SGS), Snow Particle Shape (SPS) and Specific Surface Area (SSA) under cloud-free conditions. This is the first part of the paper, to describe the retrieval method and the sensitivity study. Nine pre-defined SPSs (aggregate of 8 columns, Drontal, hollow bullet rosettes, hollow column, plate, aggregate of 5 plates, aggregate of 10 plates, solid bullet rosettes, column) are used to describe the snow optical properties. The optimal SGS and SPS are estimated iteratively utilizing a Look-Up-Table (LUT) approach. The SSA is then calculated using another pre-calculated LUT for the retrieved SGS and SPS. The optical properties (e.g., phase function) of the ice crystals can reproduce the wavelength-dependent/angular-dependent snow reflectance features, compared to laboratory measurements. A comprehensive study to understand the impact of aerosol, SPS, ice crystal surface roughness, cloud contamination, instrument spectral response function, snow habit mixture model, and snow vertical inhomogeneity on the retrieval accuracy of snow properties has been performed based on SCIATRAN radiative transfer simulations. The main findings are (1) Snow angular and spectral reflectance feature can be described by the predefined ice crystal properties only when both SGS and SPS can be optimally and iteratively obtained; (2) The impact of ice crystal surface roughness plays minor effects on the retrieval results; (3) SGS and SSA show an inverse linear relationship; (4) The retrieval of SSA assuming non-convex particle shape, compared to

29 convex particle (e.g. sphere) shows larger results; (5) Aerosol/cloud contamination due to

30 unperfected atmospheric correction and cloud screening introduces underestimation of SGS,

31 "inaccurate" SPS and overestimation of SSA; (6) The impact of   instrument spectral response

32 function introduces an overestimation on retrieved SGS, an underestimation on retrieved SSA

33 and no impact on retrieved SPS; (7) The investigation, by taking a ice crystal particle size

34 distribution and habit mixture into account, reveals that XBAER retrieved SGS agrees better

35 with the mean size, rather than the mode size for a given particle size distribution.

37 **1 Introduction**

38 Snow properties such as snow albedo, Snow Grain Size (SGS), Snow Particle Shape (SPS),

39 Specific Surface Area (SSA), snow purity (Warren and Wiscombe, 1980; Painter et al., 2003;

40 Hansen and Nazarenko, 2004; Taillandier et al., 2007; Gallet et al., 2009; Battaglia et al., 2010;

41 Gardner et al., 2010; Domine et al., 2011; Liu et al., 2012; Qu et al., 2015; Baker et al., 2019;

42 Pohl et al., 2020a) show large variabilities temporally and spatially (Kukla et al., 1986). They

43 play important roles in the global radiation budget, which is critical to some well-known

44 phenomenon such as the Arctic amplification (Serreze and Francis, 2006; Domine et al., 2019).

45 Satellites offer an effective way to understand the surface-atmosphere processes and

46 corresponding feedback mechanisms on the regional, continental and/or global scales (Konig

47 et al., 2001; Pope et al., 2014). Satellite derived snow products (e.g., SGS, SPS, and SSA) are

48 particularly important for short-term hydrological, meteorological and climatological

49 modelling (Livneh et al., 2009). A high-quanlity snow property data product can also be applied

50 to derive Aerosol Optical Thickness (AOT) over cryosphere (Mei et al., 2020a). High-quality

51 satellite derived snow products and their by-products are also important for the creation of long-

52 term "Climate Data Records" (SSMC, 2014), which enable a better investigation and

53 interpretation concerning global climate change (Konig et al., 2001). However, both the

54 definition and the corresponding data accuracy of SGS are poor (Langlois et al., 2020) while

55 there is no existing SPS satellite product. The lack of good information on SGS and SPS leads

56 to low quality of SSA (Gallet et al., 2009). The accuracy of SGS, SPS and SSA limits the model

57   performance for the prediction of snow properties related to climate change issues. Lack of

58   information of SGS and SPS also restricts the accuracy of snow bidirectional reflectance

59   estimation, which further limits the retrieval possibilities of aerosol and cloud properties above

60   snow (Mei et al., 2020a, 2020b).

61   A comprehensive overview of remote sensing of SGS, SPS, and SSA can be found in

62   many previous publications (e.g., Li et al., 2001; Stamnes et al., 2007; Koren, 2009; Lyapustin

63   et al., 2009; Dietz et al., 2012; Wiebe et al., 2013; Frei et al., 2012; Mary et al., 2013;

64   Kokhanovsky, et al., 2019; Xiong et al., 2018). The variation of SGS leads to the large

65   variability of Top Of Atmosphere (TOA) reflectance in NIR/SWIR spectral ranges while SPS

66   shows a strong impact on TOA reflectance at visible channels (Warren and Wiscombe, 1980).

67   Different retrieval algorithms have been developed for different instruments. For instance, the

68   MODIS Snow Covered-Area and Grain size (MODSCAG) retrieval algorithm and Multi-Angle

69   Implementation of Atmospheric Correction (MAIAC) algorithm have been used to derive SGS

70   using MODIS and VIIRS instruments (Painter et al., 2003; 2009; Lyapustin et al., 2009).

71   Snow particle shape is another important parameter which affects the estimation of snow

72   properties, such as albedo (Räisänen et al., 2017; Flanner and Zender, 2006), because ice

73   crystals with different shapes have different optical properties (Jin et al., 2008; Yang et al.,

74   2013). The absorption and extinction cross-sections of an ice crystal can be described as a

75   function of size, shape, and refractive index at a given wavelength (van de Hulst 1981;

76   Mischenko et al., 2002 and references therein). Natural snow consists of grains, depending on

77   temperature, humidity, and meteorological conditions, which have numerous different shapes

78   (Nakaya, 1954). SPSs have been classified into different categories, the classification has been

79   increased from 21 (Nakaya and Sekido, 1938) to 121 categories (Kikuchi et al., 2013). Although

80   spherical shape assumption is typically used for field measurements (Flanner and Zender, 2006;

81   Donahue et al., 2020), this approximation is not recommended to be used in retrieval algorithms

82   of satellite measurements because it leads to large differences between observed and simulated

83   wavelength-dependent snow bidirectional reflectance, especially at visible wavelengths

84   (Leroux and Fily et al., 1998; Aoki et al., 2000; Jin et al., 2008; Dumont et al., 2010; Libois et

85   al., 2013). Improper wavelength-dependent snow bidirectional reflectance caused by a

86 predefined SPS leads to low-quality satellite retrieval results. Some attempts to derive SPS in

87 the ice cloud can be found in previous publications (McFarlane et al., 2005; Cole et al., 2014).

88 According to Legagneux et al., (2002), SSA is defined as the surface area of ice crsytal

89 per unit mass, i.e., SSA = $A_t/\rho V$, where A_t and V are total surface area and volume, respectively,

90 ρ is the ice density. SSA includes information on both SGS and SPS and it is often used to

91 describe the surface area available for chemical processes (Taillandier et al., 2007; Domine et

92 al., 2011; Yamaguchi et al., 2019). SSA is reported to have a good relationship with snow

93 spectral albedo at the short wave infrared wavelengths (Domine et al., 2007). Optical methods

94 are routinely used to measure SSA in the field (Gallet et al., 2009). Empirical equations have

95 been proposed to describe the change of SSA (Legagneux and Domine, 2005; Taillandier et al.,

96 2007). Few attempts have been made to derive SSA from satellite observations (Mary et al.,

97 2013; Xiong et al., 2018).

98 This paper presents a new retrieval algorithm to derive SGS, SPS, and SSA from satellite

99 observations. In a snow-atmosphere system, satellite observed TOA reflectances are affected

100 by numerous snow and atmospheric parameters. The parameters, which will be estimated in the

101 framework of the eXtensible Bremen Aerosol/cloud and surfacE parameters Retrieval (XBAER)

102 algorithm, will be called the target parameters. Other parameters, which the TOA reflectance

103 also depends on, will be called the model parameters. In the case of the XBAER algorithm, the

104 target parameters are SGS, SPS, and SSA, whereas the model parameters are aerosol loading,

105 cloud optical thickness, and gaseous absorption. Throughout the paper, SGS will be

106 characterized by an effective radius. Following Baum et al., (2011), the effective radius is

107 defined as $3V/(4A_p)$, where V and A_p are the volume and average projected area, respectively.

108 As can be seen, in the case of a spherical particle, the effective radius is equal to the radius of

109 the sphere. The general concept of the retrieval algorithm is to use simultaneously spectral and

110 angular reflectance measurements, which are sensitive to SGS and SPS. The spectral channels

111 used in the XBAER algorithm are 0.55 μm and 1.6 μm. Both nadir and oblique observation

112 directions from SLSTR are used. An optimal SGS and SPS pair is achieved by minimizing the

113 difference between measured and simulated atmospheric-corrected surface reflectances. SSA

114 is then calculated based on the retrieved SGS and SPS. Nine predefined SPSs (aggregate of 8

columns, droxtal, hollow bullet rosettes, hollow column, plate, aggregate of 5 plates, aggregate of 10 plates, solid bullet rosettes, column) (Yang et al., 2013, see Table 1) are used to describe the snow optical properties and to simulate the snow surface reflectance at 0.55 and 1.6 μm at two observation angles.

Three points we would like to emphasize to avoid misunderstandings between snow science community and remote sesning community.

- ➢ **Usage the Yang et al (2013) database for ice crystal in the air (ice cloud) and on the ground (snow).** The optical properties of ice crystals presented by Yang et al., (2013) have been widely used to study ice clouds. In recent publications, it has been demonstrated that they can also be used for snow studies (Räisänen et al, 2015; Pirazzini et al., 2015; Saito et al., 2019; Schneider et al., 2019; Pohl et al., 2020b). In fact, the single-scattering properties of ice crystals in Yang et al., (2013) database are determined solely by given particle size, shape, and refractive index. They can be used to describe the optical properties of both snow particles and ice cloud particles when the particle models represent the aforementioned optical/physical properties (Saito et al., 2019; Personal communication with Dr. Saito).

- ➢ **Snow particle shape observed from field measurements and derived from satellite observations**. For scientists working in a laboratory or on campaign-based studies, the best way to get an image of snow is to use an X-ray microtomography or confocal scanning optical microscope/scanning electron microscope (Hagenmuller et al., 2016; Baker et al., 2019; Personal communication with Dr. Ian Baker). In a field measurement and its related application areas (e.g., calculation of snow albedo), a spherical shape assumption is widely used because it is easier to derive other snow properties such as SSAs and snow albedo based on this assumption, compared to other more complicated shapes (see Appendix). The assumption of spherical and non-spherical shape has much less impact on the estimation of snow albedo compared to the bidirectional reflection features of snow (Grenfel and Warren, 1999; Dumont et al., 2010). Because SPS has a significant impact on the ice crystal phase function

while it has a relatively weak impact on the snow extinction/absorption coefficient (Jin et al., 2008). However, the spherical shape cannot be used to provide typical bidirectional reflection features of snow with required accuracy (Jin et al., 2008; Dumon et al., 2010; Jiao et al., 2019), which is the fundamental basis to derive snow properties from satellite remote sensing techniques. Thus, more complicated SPSs, such as those proposed by Yang et al (2013), are recommended to use in the simulations of the angular distribution of snow reflectance. Besides, both snow albedo and directional reflectance are affected by other factors such as how single particle aggregates;

> **SGS and SSA**. Although the definition of snow grain constitutes is an ongoing debate in different communities, SGS and SPS are two fundamental inputs for any radiative transfer model, which is the basis for the satellite retrievals (Langlois et al., 2020). Typically, the SSA is more preferable within the snow science community because SSA is commonly used in further applications based on field measurements. We note, however, according to the definition of SSA, for a given SPS, a unique relationship between SGS and SSA can be derived. SPS is the intermediate but fundamental parameter needed to retrieve SSA in our XBAER algorithm.

This paper is structured as follows: observations characteristics of SLSTR and the laboratory measurements used for sensitivity studies are described in section 2. The theoretical background and the ice crystal database (Yang et al., 2013) are presented in section 3. Section 4 describes the eXtensible Bremen Aerosol/cloud and surfacE parameters Retrieval (XBAER) algorithm. The results of a comprehensive sensitivity study using SCIATRAN (Rozanov et al., 2014) simulations are presented in section 5. The conclusions are given in section 6.

Table 1 Snow particle shape provided in Yang et al (2013) database. The abbreviations are introduced here will be used later

Snow particle shape	Abbreviation	Schematic drawing
Aggregate of 8 columns	col8e	
Droxtal	droxa	
Hollow bullet rosettes	holbr	
Hollow column	holco	
Plate	pla_1	
Aggregate of 5 plates	pla_5	
Aggregate of 10 plates	pla_10	
Solid bullet rosettes	solbr	
Column	solco	

170

171

172

173 **2 Data**

174 **2.1 SLSTR instrument**

175 The satellite data will be used twofold throughout the paper. In the first part, we perform a

176 statistical analysis of the SLSTR observation/illumination geometries to select realistic settings

177 for the sensitivity study. In the second part of the companion paper, the satellite measurements

178 will be used as the inputs of the XBAER algorithm to derive the research satellite products of

179 SGS, SPS, and SSA.

180   The SLSTR instrument onboard the European Space Agency (ESA) satellite Sentinel-3 is the

181   successor of the Advanced Along-Track Scanning Radiometer (AATSR) instrument, which is used

182   to maintain continuity with the (A)ATSR series of instruments. SLSTR takes the heritage of AATSR

183   instrument characteristics, especially the dual-viewing observation capabilities and wavelength

184   settings. In order to have a reasonable setting for observation/illumination geometries in the

185   sensitivity study, we perform a statistical analysis of the SLSTR observation geometries (solar

186   zenith angle, SZA, viewing zenith angle, VZA, relative azimuth angle, RAA), similar as Mei et al

187   (2020a). This analysis is essential because 1) it provides a realistic setting of

188   observation/illumination geometries in our sensitivity studies; 2) it helps us to have a complete

189   understanding of the observation/illumination related surface/atmospheric properties. Here the

190   definition of RAA has been harmonized with SCIATRAN (Rozanov et al., 2014), namely, RAA

191   value is equal to 0° under strict glint condition. The statistical analysis has been performed using

192   observations over Greenland during April and September 2017. April and September are reported

193   to be representativeness months of the Arctic (Mei et al., 2020a). Please be noted that these two

194   months are picked up to represent the SLSTR observation characteristic with typical solar

195   illumination angle, the change of underlying surface properties plays no role in such selection. Fig.

196   1 shows the frequency of SLSTR observation geometries. The upper panel shows the SZA with

197   SLSTR nadir and oblique observations for April and September. We can see that the SZA occurs

198   frequently with a value of 70° for selected months. The VZA and RAA for oblique observation mode

199   are typically around 55° and in a range of [110°, 170°], respectively. The observation geometries

200   for nadir observation show relatively large variabilities due to larger swath width compared to

201   oblique (1400 km vs 700 km). Larger SZA can be found especially at the edge of the swath. The

202   VZA and RAA for oblique observation mode are typically in ranges of [0°, 55°] and [70°, 140°],

203   respectively. According to the statistical analysis, a combination of SZA, VZA, RAA of 70°, 30°,

204   135° for nadir observation and 70°, 55°, 135° for oblique observation can be a reasonable setting

205   for the SLSTR observation geometries for the sensitivity study.

206
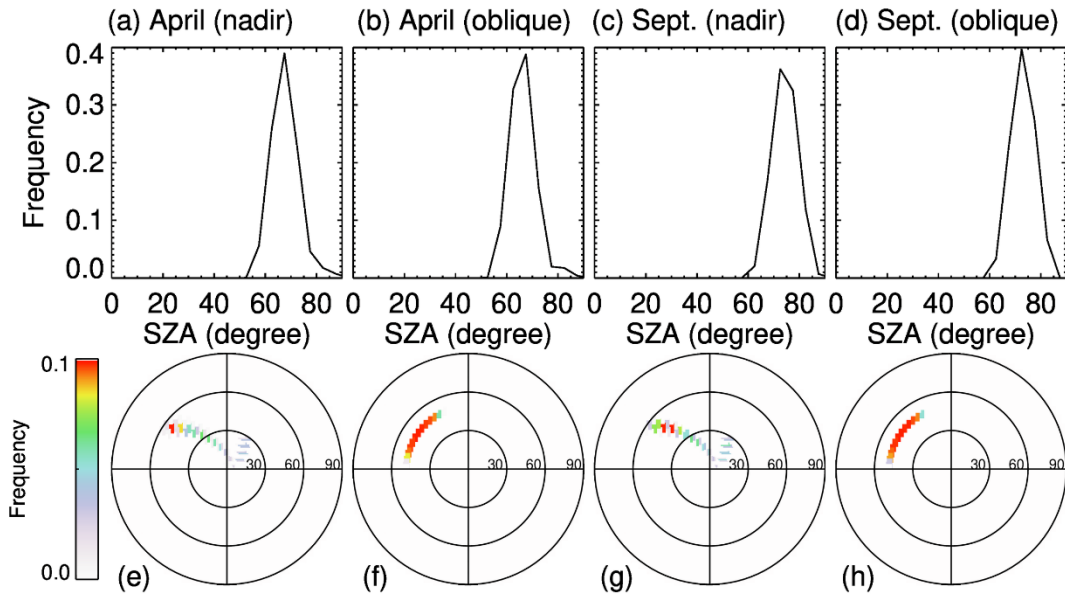
207

208 Fig. 1 Upper panel is the histograms of SZA for SLSTR observations: (a) nadir during April;

209 (b) oblique during April, (c) nadir during September; (d) oblique during September. Lower

210 panel is the polar plots of (VZA, RAA) probability for AATSR observations: (e) nadir during

211 April; (f) oblique during April, (g) nadir during September; (h) oblique during September.

212

2.2 Laboratory measurements

214 Laboratory measurements of the bidirectional reflectance of snow samples contain important

215 information about the dependence of the angular structure of snow reflection on the lighting

216 geometry, wavelength, and snow physical properties. The comparison of measured and

217 modeled bidirectional reflectance helps to establish the conceptual ideas for the retrieval

218 algorithm. For this comparison, we have selected measurements of fresh and aged snow

219 samples presented by Dumont et al., (2010) and Peltoniemi et al., (2009), respectively.

220   The fresh snow sample, a cylinder of 30 cm diameter and 12 cm height, was taken from

221 new wet snow layer at Col de Porte (Chartreuse, France) at 1300 meter above sea level during

222 January 2008 (Dumont et al., 2010). The sample was stored in a cold room at -10°C for one

223 week to avoid metamorphic effects during the ensuing measurements. To obtain the

224 Bidirectional Reflectance Factor (BRF), the snow sample was illuminated by a monochromatic

225 light source at incidence zenith angle of 60°. The spectral BRF between 500 and 2600 nm was

226 measured at viewing zenith angles of 0°, 30°, 60°, 70° and relative azimuth angles 0°, 45°, 90°,

227 135°, 180° by a spectrogonio-radiometer developed at the Laboratoire de Planétologie de

228 Grenoble, France, and using a Spectralon® and an infragold® sample as a reference (see

229 Dumont et al., (2010) for further details).

230   The aged snow sample, a cuboid of more than 10 cm height, was taken from an old dry

231 snow layer at Masala, Finland, and brought into a warm laboratory. The spectral BRF between

232 350 and 2500 nm was measured during the aged process by the Finnish geodetic institute field

233 goniospectro-polariphotometer (FIGIFIGO) and using a Labsphere Spectralon 99% white

234 reference plate. For illumination, a 1000 W Oriel Research Quartz tungsten halogen lamp at a

235 zenith angle of 60° was utilized (Peltoniemi et al., 2009). Spectral BRF was obtained at viewing

236 zenith angles up to 70° in 1° resolution and at relative azimuth angles of 0°, 90°, 130°, 160°,

237 180°, 270°, 310°, and 340°. The first and last measurements were done in the principal plane,

238 indicating minor metamorphism in the snow layer during the measurement.

239

240

241 **3 Dependence of snow reflectance on target parameters**

242 A comprehensive data library (Yang et al., 2013) containing the scattering, absorption, and

243 polarization properties of ice particles in the spectral range from 0.2 to 15 μm was used to

244 calculate radiative transfer through a snow layer (Pohl et al., 2020b). A full set of single-

245 scattering properties is available for nine ice crystal habits presented in Table 1. The maximum

246 dimension of each habit ranges from 2 to 10000 μm in 189 discrete sizes.

247   The optical properties of ice crystals depend on wavelength, ice crystal size, and shape.

248 Maximal dependence of the single-scattering albedo on the particle size is observed in the

249 spectral ranges where ice absorption cannot be neglected. The asymmetry factor depends on

250 the particle size for the whole spectral range. This dependence can be weaker or stronger at a

251 selected wavelength depending on SPS (see Yang et al., (2013) for details).

252   To better illustrate the impact of SGS and SPS on the radiative transfer through a snow

253 layer, we have calculated the reflectance of the snow layer consisting of droxtals, aggregates of

254 8 columns, hollow columns, and plates with crystal surface roughness condition as severely

255 roughened. The simulations of snow reflectance were performed using the radiative transfer

256 package SCIATRAN (Rozanov et al., 2014). The snow layer was defined as a layer directly

257 over a black surface, with snow optical thickness of 500 and a snow geometrical thickness of

258 1m. The snow layer is assumed to be vertically and horizontally homogeneous without any

259 surface roughness and composed of monodisperse ice crystals. The impact of snow impurities

260 and scattering/absorption processes in the atmosphere was neglected at this stage. The

261 reflectance of the snow layer as a function of the effective radius of ice crystal at wavelengths

262 0.55 μm and 1.6 μm is presented in Fig. 2. The calculations were performed for typical SLSTR

263 instrument observation/illumination geometries (see section 2.1), with SZA, VZA, and RAA

264 equal to 70°, 30°, and 135° (scattering angle 129°).

265   There are a couple of criteria we considered for the selection of the optimal wavelengths

266 (0.55 μm and 1.6 μm) in XBAER algorithm, for the purpose of creating a long-term satellite

267 snow properties dataset with good and stable accuracy.

268   ➢   Taking the overlap channels between AATSR and SLSTR because a consistent

269   long-term satellite snow dataset is possible only when the same algorithm can be

270   applied on both AATSR and SLSTR instruments. In particular, the overlap channels

271   between AATSR and SLSTR are 0.55, 0.66, 0.87, 1.6, 3.7, 10.85, and 12μm.

272   ➢   Picking up wavelengths, for which contribution of thermal emission can be

273   ignored, then 0.55, 0.66, 0.87, and 1.6 μm remain.

274   ➢   Deleting the channel 0.66μm to avoid the potential impact of O_3 absorption,

275   after that, 0.55, 0.87, and 1.6 μm remain.

276   ➢   Taking into account, that the retrieval algorithm is a two-stage algorithm, namely,

277   first it uses channels with minimum impact of ice crystal shape to retrieve the grain

278   size, and then it selects the shape using channels with minimum impact of grain size.

279   Accounting for that the channel 0.87μm is impacted by both size and shape, 0.55 and

280   1.6μm channels were picked up for the retrieval.

281   The right panel of Fig. 2 demonstrates the strong dependence of the snow layer reflectance

282 at 1.6 μm on the SGS. One can also see that the dependence of snow reflectance on SPS cannot

283 be neglected. In particular, the same reflectance can be obtained with a combination of different

284 SGS and SPS. For instance, one can see from the right panel of Fig. 2 that, the reflectance of

285 the snow layer consisting of droxtals with SGS=200 μm or of plates with SGS=65 μm equals

286 ~0.035 in both cases. Thus, assuming different SPSs, the values of retrieved SGS can differ 3

287 times.The left panel of Fig. 2 demonstrates the dependence of the snow layer reflectance at 0.55

288 μm on SGS and SPS. It can be seen that the dependence of reflectance on SGS is very weak for

289 droxtals and aggregate of 8 columns. However, reflectance at 0.55 μm decreases with an

290 increase of SGS for hollow columns and plates. The weak oscillations for the reflectances at

291 0.55 μm can be explained by the joint impact of oscillations in the single-scattering albedo and

292 elements of the scattering matrix presented in the original database. Although the reason for the

293 oscillation in the database is unclear, it is unlikely due to physical phenomena (Dr. M. Saito ,

294 personal communication).
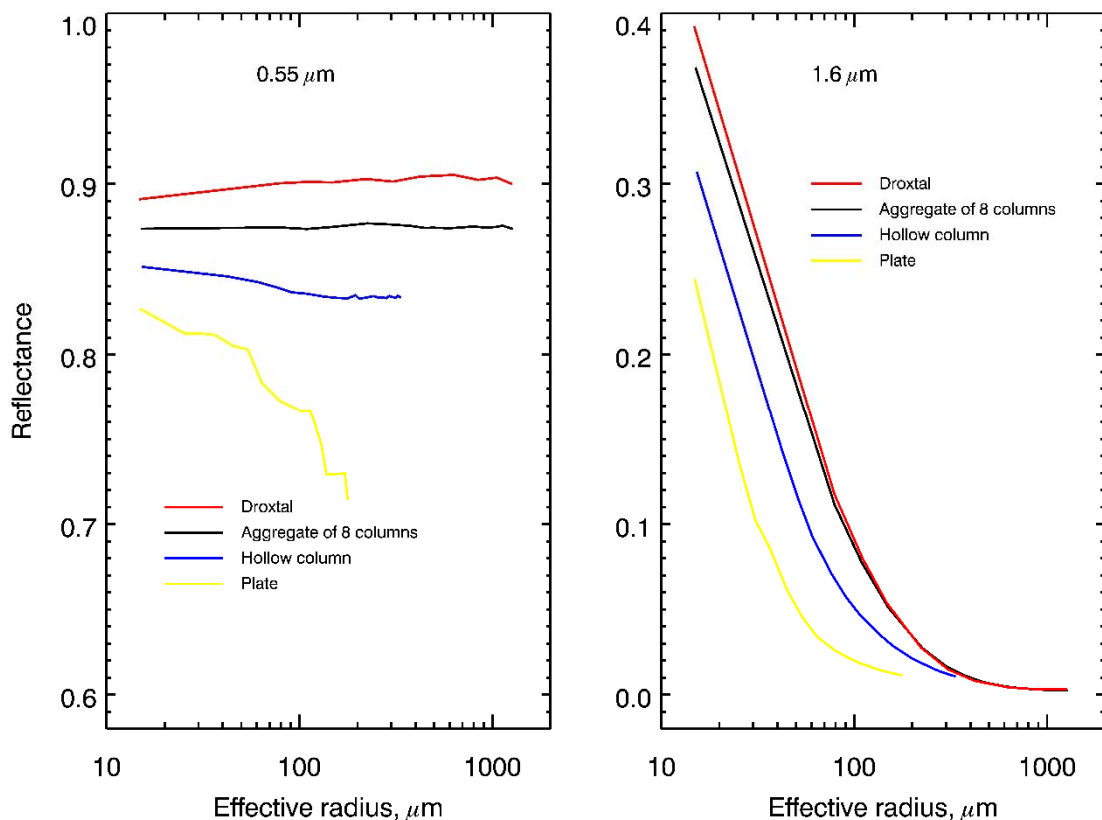
295

296 Fig 2. Reflectance of snow layer at 0.55 μm and 1.6 μm calculated assuming different SPS.

297 Observation/illumination geometry: SZA, VZA and RAA were set to 70°, 30° and 135°,

298 respectively.

299   To illustrate this point, the dependence of the phase function at 129° scattering angle on

300   SGS is shown in the left panel of Fig. 3. The phase functions (F11 element of the scattering

301   matrix) were extracted from the original database. According to the left panel of Fig. 3, the

302   dependence of snow surface reflectance at 0.55 μm on SGS and SPS is caused mainly by the

303   phase function of ice crystal. Weak oscillations can also be found.

304   The above analysis shows that accurate retrieval of SGS requires adequate information

305   about SPS and accounting for the dependence of the phase function on SGS. To better illustrate

306   the impacts of SGS on ice crystal phase function, we calculated reflectance at 1.6 μm with

307   different SGS values. The right panel of Fig. 3 represents the reflectance of the snow layer,

308   consisting of aggregates of 8 columns, calculated accounting for the dependence of the phase

309   function on the effective radius (black line) and assuming constant phase function for three

310   selected effective radii equal to 15, 150, and 1150 μm (red, green, and blue lines, respectively).

311   It can be seen that the accurate simulation of snow reflection requires accounting for the

312   dependence of phase function on SGS.

313   The main findings of presented investigations can be formulated as follows:

314   ➢   reflectance of a snow layer depends on both SGS and SPS;

315   ➢   accurate simulation of snow surface reflectance requires accounting for the dependence of

316   phase function on SGS;

317   ➢   spectral channels in the visible spectral range is more sensitive to SPS compared to SGS;

318   ➢   spectral channels in the near infrared spectral range is more sensitive to SGS compared to

319   SPS.

320

321

322
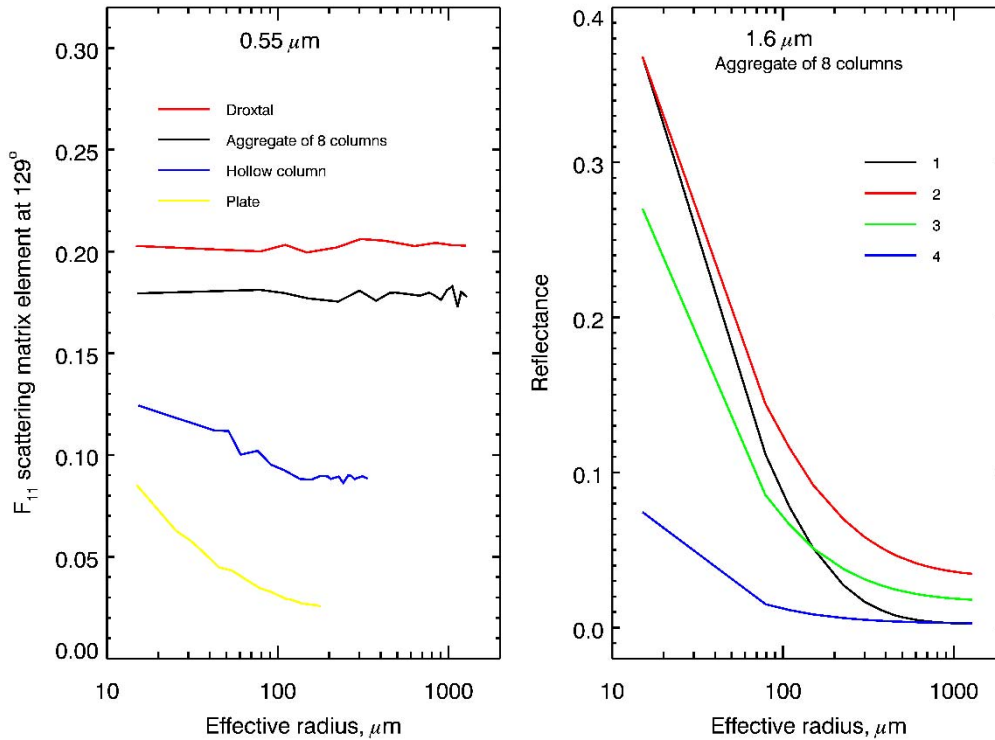
Fig 3. Left panel: phase function at 0.55 μm for scattering angle of 129°, extracted from the original database (Yang et al., 2013) as a function of effective radius. Right panel: reflectance of snow layer at 1.6 μm consisting of aggregate of 8 columns, calculated assuming that: 1: phase function depends on the effective radius (black line); 2: phase function is constant corresponding to the effective radius 15μm (red line); 3: same as 2 but for effective radius of 150 μm (green line); 4: same as 2 but for effective radius of 1150 μm (blue line).

329

Although the global classification snow crystal, ice crystal, and solid precipitation particles suggested in Kikuchi et al. (2013) consist of the 121 particle types, we restrict ourselves, in the retrieval algorithm, with nine shapes of ice crystals, for which optical characteristics are represented in database (Yang et al., 2013). And these nine shapes have been proven to be used to reproduce typical wavelength/angular features of snow reflectance in reality, especially from satellite observations (Räisänen et al, 2015; Pirazzini et al., 2015; Saito et al., 2019; Schneider et al., 2019; Pohl et al., 2020b). To futher illustrate that the selected dataset is able to reproduce the BRF of different snow types, we compared the simulated and measured BRF of fresh (Dumont et al., 2010) and aged (Peltoniemi et al., 2009) snow samples.

339   To reproduce the spectral BRF by SCIATRAN, we use the setup described above in this section

340   and adjust the SGS for each SPS by minimizing the deviation between simulated and measured

341   reflectance at 1.6 μm. Figure 4 shows the simulated BRF in the principal plane at 0.55 μm of

342   fresh and aged snow samples, as well as the respective measurements. The BRF is defined as

343   πI/F, where I is the reflected radiance and F is the incident irradiance. According to Fig. 4(a),

344   for fresh snow, plates are the best shape to reproduce the measured BRF in the vicinity of the

345   forward scattering peak but plates underestimate the BRF at higher viewing zenith angles in the

346   backscattering region. Here, shapes of hollow bullet rosette, hollow column, aggregate of 10

347   plates exhibit better potential to simulate the fresh snow layer BRF. In the case of aged snow,

348   shapes of solid and hollow column, hollow bullet rosette, and aggregate of 5 and 10 plates

349   provide BRF values in conformity with respective measurements. However, they slightly

350   underestimate the BRF at high zenith angles in the backscattering region where aggregate of 8

351   columns can simulate the aged snow BRF better.
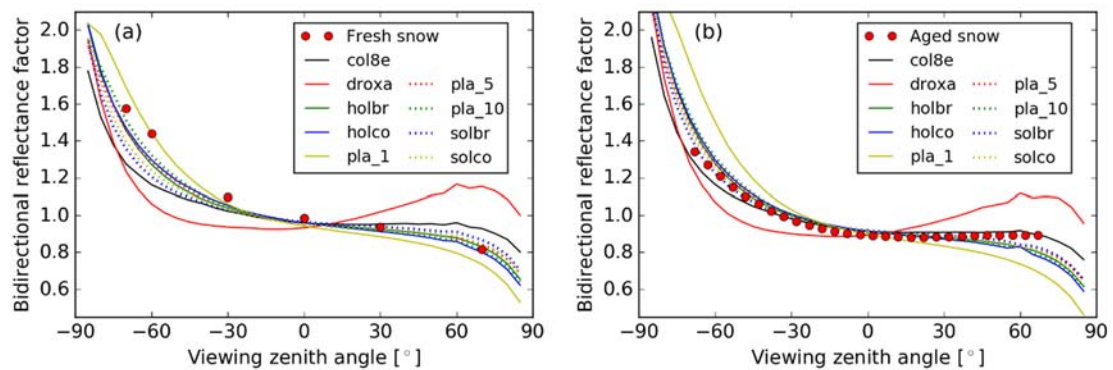
352

353   Fig. 4 The comparison of angle dependence of laboratory-measured and simulated snow

354   reflectance: (a) fresh snow sample; (b)aged snow sample. Symbols - measurements, lines –

355   simulations with SCIATRAN assuming different SPS (see legend).

356   The above analysis demonstrates that the selected database of SPS can be used

357   successfully to reproduce measured BRF of both fresh and aged snow samples. Similar results

358   were obtained by Pohl et al., (2020b). In this paper, top of atmosphere BRF at 865 nm derived

359   from POLarization and Directionality of the Earth's Reflectances 3 (POLDER-3) on

360   Polarization & Anisotropy of Reflectances for Atmospheric Sciences coupled with

361   Observations from a Lidar (PARASOL) measurements over a pure snow surface in Greenland

362 (70.5° N, 47.3° W) on 6 July 2008 were compared with the SCIATRAN simulations, using

363 droxtals, solid bullet rosettes, and solid columns.

364 According to the above analysis, we can formulate the general algorithm to retrieve SGS

365 and SPS from satellite observations. Satellite provides the wavelength-dependent TOA

366 reflectance, for a given SGS and SPS pair, the minimization between satellite observed TOA

367 reflectance and theoretical simulation is performed. The optimal SGS and SPS are obtained

368 when the difference between observations and simulations reaches the predefined criteria. The

369 SSA is then calculated by the retrieved SGS and SPS.

370

371 **4 XBAER Algorithm**

372 The retrieval algorithm consists of three stages. The first stage includes the estimation of

373 SGS using the effective Lambertian surface albedo after atmospheric correction for selected

374 observation geometries and wavelengths. This step is performed based on the path radiance

375 representation (Mei et al., 2017), in which the TOA reflectance can be described by the

376 contribution from the atmosphere and the interaction between atmosphere and surface. The

377 inverse to derive the surface reflectance from the satellite observed TOA reflectance is called

378 the atmospheric correction. And due to certain assumptions in the path radiance

379 representation, the derived surface reflectance is equivalent to the effective Lambertian

380 surface albedo. The estimation of SGS is obtained solving the following minimization

381 problem with respect to the effective radius, *r*, of snow crystals:

382 $$\left\| A_e - \boldsymbol{R}_s(r) \right\|^2 \rightarrow \min. \tag{1}$$

383 Here, $\mathbf{A}_e$ and $\mathbf{R}_s(r)$ are two vectors which components are the effective Lambertian

384 surface albedo and the simulated snow reflectance, respectively. The dimension of these

385 vectors is the number of wavelengths times the number of viewing directions.

386 The simulation of snow reflectance (components of vectors $\mathbf{R}_s(r)$) was performed using

387 the radiative transfer package SCIATRAN (Rozanov et al., 2014) as described in Section 3.

388   The optical properties of nine SPSs, listed in Table 1, were used for radiative transfer

389   calculations.

390   The minimization problem formulated by Eq. (1) was solved separately for each SPS

391   using Brent's method (Brent, 1973). The solution of the minimization problem for each

392   crystal habit is characterized by the following residual:

393    $\Delta_i = \left\| A_e - R_s(r_i^*) \right\|^2, i = 1, 2, ..., 9,$ (2)

394   where r_i^* is the solution of minimization problem given by Eq. (1) for i^{th} shape of the ice

395   crystal particle.

396   The second stage is the selection of such i (SPS) for which Δ_i is minimal. This

397   completes the retrieval process and enables the optimal SGS and SPS to be obtained.

398   The third stage is to calculate SSA for the retrieved SGS and SPS. To this end, let us

399   rewrite the SSA introduced above in the following equivalent form:

400        $SSA = 3/\rho r \cdot (A_t/4A_p),$ (3)

401   where r is the effective radius. According to Cauchy's surface area formula (Cauchy, 1841;

402   Tsukerman and Veomett, 2016), the average area of the projections of a convex body is

403   equal to the surface area of the body, up to a multiplicative constant. In our case, this results

404   in $A_t = 4A_p$ and SSA for convex particles such as droxtals, solid columns, and plates are

405   equal to $3/\rho r$. In the case of non-convex particles, the calculation of SSA requires the

406   information about total area A_t. Although the database given by Yang et al. (2013) does not

407   contain information about A_t, the total area of non-convex particles can be calculated

408   employing geometric parameters of ice crystal habits presented in Table 1 of Yang et al.

409   (2013). Here we take a typical SPS, aggregate of 8 columns, as an example, to show the

410   difference between SSA calculated assuming convex and non-convex particle.

411   According to M. Saito (private communication), the parameters L and a of the

412   aggregate of 8 columns (see Fig. 3 in Yang et al (2013) for details) can be obtained by

scaling with respect to the maximum dimension, D. To find these values for different maximal dimensions, we calculate at first the volume of aggregate of 8 columns corresponding to parameters a and L on a relative scale as given in Table 1 of Yang et al (2013).

$$V_r = \frac{3\sqrt{3}}{2} \sum_{i=1}^{8} a_i^2 L_i. \tag{4}$$

Using the database of Yang et al (2013), one can obtained the maximal dimension, D_r, corresponding to the volume, V_r. Introducing the scaling factor, $C_k = D_k/D_r$, we have semi-width and length for the aggregate with the maximal dimension D_k:

$$a_{i,k} = a_i C_k, \quad L_{i,k} = L_i C_k. \tag{5}$$

The total surface of the aggregate on relative scale is given by

$$S_r = 3 \sum_{i=1}^{8} (\sqrt{3} a_i^2 + 2 a_i L_i). \tag{6}$$

Accounting for Eq (5), we have

$$S = C_k^2 S_r. \tag{7}$$

Having obtained the total area, one can calculate SSA as the total surface area of a material per unit of mass:

$$SSA = \frac{S}{\rho V} = \frac{S_r}{\rho C_k V_r}. \tag{8}$$

Comparing SSA of convex particle equal to $3/\rho r$ with result given by Eq. (8), one can easily notice the difference of SSA calculated from different SPS using the same SGS. The details of such calculations for other non-convex ice crystal habits are given in the Appendix.

432   The relationship between SSA and SGS for different SPS is presented in Fig. 5. According

433   to Fig. 5, an almost inverse linear relationship between SSA and SGS can be found. The lines,

434   representing droxtal, plate, and column, are overlapped, indicating the same SSA for convex

435   particles. For other SPSs with the same SGS, SSA is larger compared to convex faceted

436   particles. SSA is restricted in the range of 0-100 m^2/kg in this investigation (Picard et al.,

437   2009).For example, for SGS=100μm, the SSA is 32.7 m2/kg for convex faceted particles,

438   whereas SSAs for aggregate of 8 columns, hollow bullet rosettes, hollow column, aggregate of

439   5 plates, aggregate of 10 plates, and solid bullet rosettes are 44.2, 43.4, 37.7, 74.4, 66.8 and

440   35.6 m^2/kg, respectively. The relative differences range from 9%-128%, depending on the SPS.

441   Taking into account the definition of SSA, one can derive the following relationship between

442   SSA convex and non-convex particles: $SSA_{nc} = SSA_c \cdot (A_t/4A_p)$, where subscript c and nc

443   denotes convex and non-convex particle, respectively. The obtained results reveal that for all

444   non-convex ice crystals under consideration $A_t/4A_p > 1$ and the ratio $A_t/4A_p$ weakly depends

445   on the SGS.

446

447
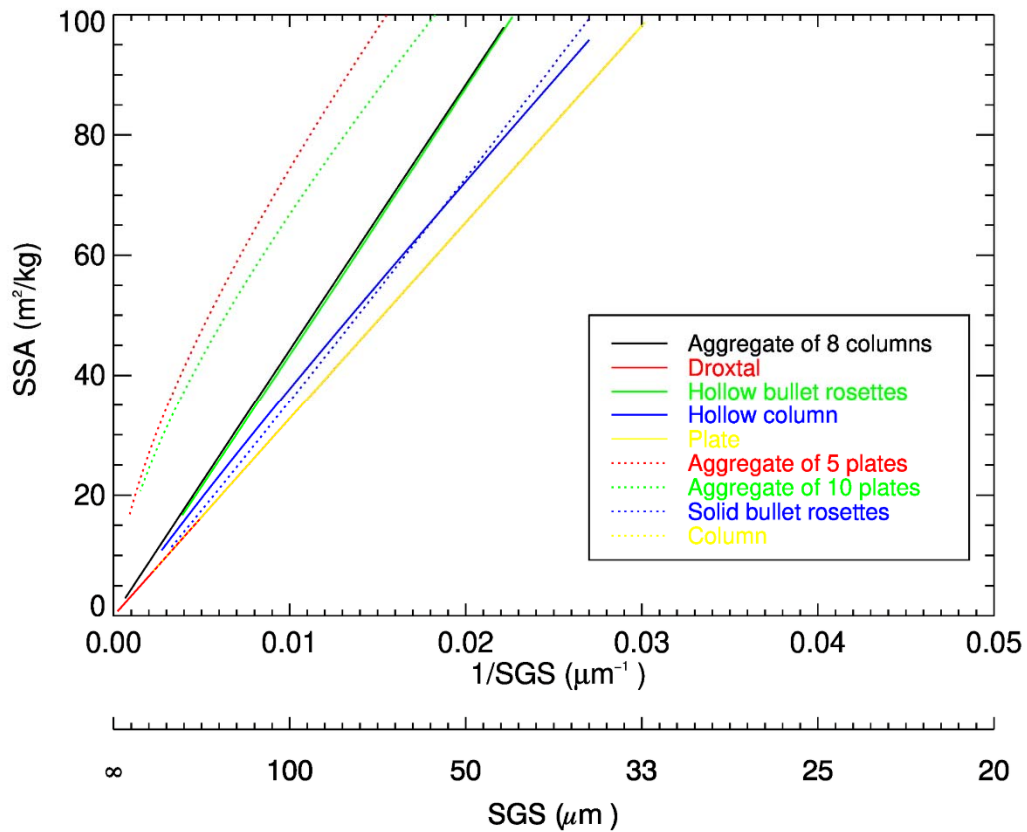
Fig 5. Relationship between SGS and SSA for different SPS. For a better illustration, the realistic range of specific surface area is limited to 100 m²/kg.

5 Impact of model parameters uncertainty

The accuracy of any retrieval algorithm depends not only on measurement errors but also on the uncertainty of parameters which cannot be retrieved. In our case, such parameters are ice crystal roughness, aerosol, and cloud contamination. The impacts of these factors on XBAER-derived SGS and SPS have been investigated and will be discussed in this section. The TOA reflectances at selected channels (0.55 and 1.6 μm) and observation directions for SZA, VZA, and RAA of 70°, 30°, and 135° for nadir 70°, 55°, and 135° for oblique, respectively, were calculated using radiative transfer model SCIATRAN. The details of each scenario will be presented in the corresponding sub-section below.

5.1 Impact of snow particle shape

Since the first stage of the XBAER algorithm is to estimate the SGS assuming a given SPS, it is reasonable to investigate the impact of SPS on the retrieval of SGS. The TOA reflectances of a snow layer at 0.55 and 1.6 μm with above-given observation geometries were calculated using the following settings for snow layer and atmospheric parameters:

➢ **Snow Layer:** consists of ice crystals with SPS set to be severely roughened aggregate of 8 columns and maximal dimensions [100, 300, 500, 700, 1000, 2000, 3000, 5000] μm, which corresponds to SGS [15, 45.1, 75.2, 105.3, 150.4, 300.8, 451.3, 752.1] μm.

➢ **Atmosphere:** excluded

The simulated snow reflectances were used as components of vector $\mathbf{A_e}$ in Eq (1). Nine SPSs from database presented in Yang et al. (2013) are used sequentially in the retrieval process. The atmospheric correction is not performed because the atmosphere is excluded in the forward simulations. This enables avoiding additional errors caused by the atmospheric correction and estimates the pure effect of SPS on the retrieval results. Fig.6 shows the impact of the SPS on SGS retrieval. Different colors and line styles indicate different ice crystals used in the retrieval process. The black solid line represents the retrieved SGS assuming SPS in the retrieval process is the same as in forward simulations. This line agrees well with the 1:1 line, indicating that the retrieval algorithm has been implemented technically correct. According to Fig.6, one can see both underestimation and overestimation of SGS depending on the SPS used in retrieval. However, in most cases, an incorrect SPS leads to an underestimation of SGS. In particular, the maximal effect can be seen when ice crystals of plate shape, rather than the correct aggregate of 8 columns, is used (yellow solid line). This result can be easily explained coming back to the right panel of Fig. 2. Indeed, one can see that the same reflectance of the snow layer can be obtained using the plate shape, instead of an aggregate of 8 columns, with significantly smaller SGS. These results reveal that the SPS is an important parameter affecting the accuracy of retrieved SGS.

490
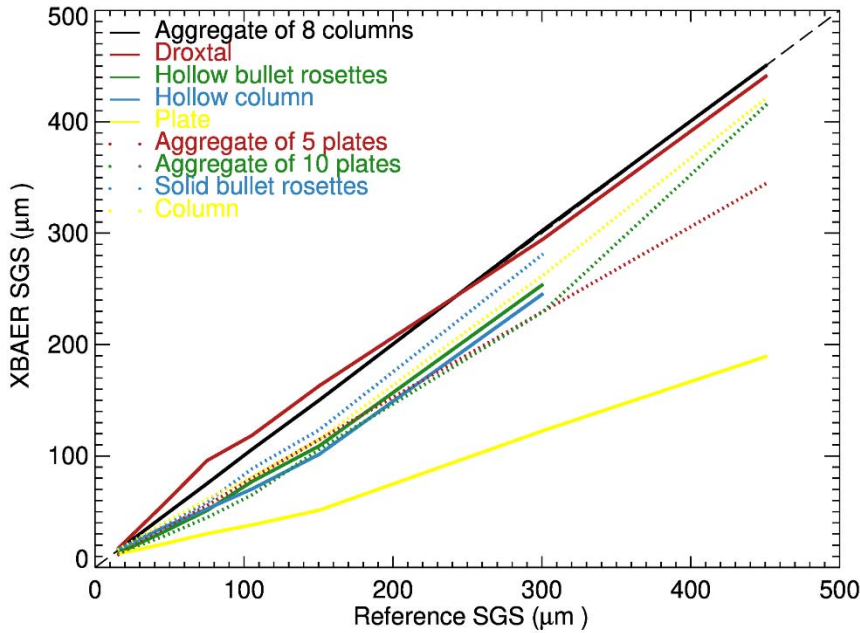
491   Fig 6. Impact of SPS on the retrieval of SGS.

492

5.2 Impact of SGS/SPS on SSA

493

494   Since the SSA is obtained from the retrieved SGS and SPS, an understanding of how the

495   error of SGS and/or SPS propagates to the SSA will provide helpful information to understand

496   the retrieved SSA. Fig. 7 shows the impact of SGS (left) and SPS (right) on XBAER retrieved

497   SSA. The relative error of SGS, $\varepsilon_r = (r - r')/r$, is propagated to the relative error of SSA as ε_{SSA}

498    $= 1 - 1/(1 - \varepsilon_r)$, and it is independent of reference SSA. The left panel of Fig. 7 depicts ε_{SSA}

499   corresponding to ± 0.16 of ε_r. One can see that this results in 19% and -13.8% of SSA relative

500   errors, which are presented as the upper and lower error boundaries in the left panel of Fig. 7.

501   The systematical error of ±16% for SGS was obtained as the maximal relative difference

502   between XBAER retrieved SGS and both *in-situ* and aircraft measured SGS (as presented in

503   the companion paper). This represents the worst case of SGS error propagation into SSA.

504   The impact of SPS on SSA is demonstrated in the right panel of Fig. 7. As a reference

505   shape, we have selected in this case the plate, which provides the same SSA as other convex

506   particles. One can see that the SSA of non-convex particles overestimates the SSA of convex

507   particles, which is in line with the results presented in Section 4. For instance, for the same

508   SGS, the SSA for aggregate 8 columns (non-convex particle) is about 3 times larger than that

509   for doxtal (convex particle). Since the assumption of the sphere (convex particle) is used to

510   measure SSA in-field measures (Gallet et al., 2009; Personal communication with Dr. Nick

511   Rutter), such as observations from SnowEx, the retrieval results of SSA from XBAER will be

512   systematically larger than field measurements in the case of non-convex particles even if the

513   retrieved and measured SGS are similar. However, a detailed discussion with respect to

514   uncertainty in the campaign-based measurement is out of the scope of this manuscript.
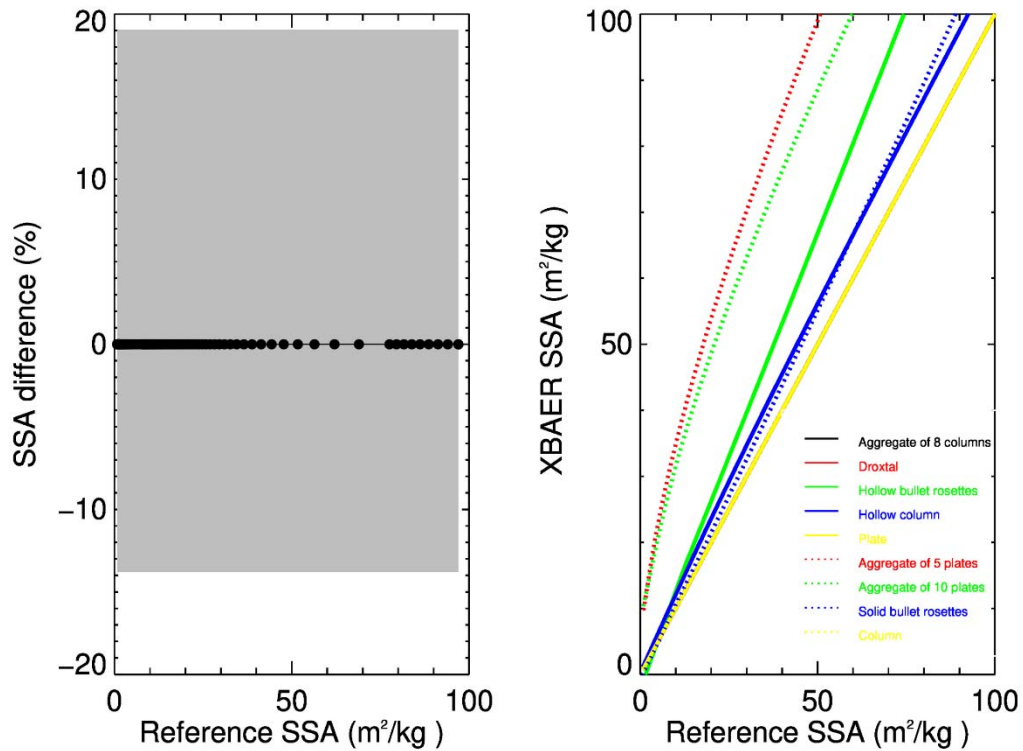
515

516   Fig 7. Impact of SGS and SPS on the retrieval of SSA. Left panel (SGS errors): the black line

517   with dots indicate the 0 difference for accurate SGS for aggregate 8 column, the grey area

518   indicate the relative error of SSA introduced by 16% error of SGS; Right panel (SPS selection):

519   different color/line styles indicate different SPS used in the calculation of SSA while the true

520   SPS is set to be „ plate" or other convex particles.

521

522

5.3 Impact of ice crystals surface roughness

Although surface roughness of ice crystal is not so severe for snow compared to ice cloud due to basic thermodynamics (Colbeck, 1980, 1983), the Ice Crystal Surface Roughness (ICSR), indicating ice crystal surface texture, may still be important for the retrieval of snow properties from optical sensors such as SLSTR. The ICSR has been used as a new variable in model simulation (Järvinen et al., 2018). Retrieval algorithms of ice cloud parameters frequently based on the assumption that the ice crystal surface is smooth (Kokhanovsky et al., 2019). This assumption can yet introduce large uncertainty in the ice cloud retrieval parameters and, as a consequence, lead to misunderstanding the impacts of ice cloud on global climate change (Järvinen et al., 2018). However, this issue has not yet been discussed for snow. In general, ice crystal surfaces are rougher in clouds than in snow layers due to metamorphism processes (Colbeck, 1980, 1983; Ulanowski et al., 2014). The investigation of the impact of ICSR on retrieval of snow properties provides valuable information to understand the XBAER algorithm. The ICSR according to Yang et al., (2013) is defined similarly as suggested by Cox and Munk (1954) for the roughness of the sea surface. A parameter σ describes the degree of ICSR. The σ values 0, 0.03, and 0.5 are for three surface roughness conditions: smooth, moderate roughness, and severe roughness. And only the above three values are available in the Yang database. The snow layer reflectances were used as components of the vector $\mathbf{A}_e$ in Eq. (1) in the same way as in Section 5.1.

Fig. 8 shows the impact of ICRS on the retrieved SGS, SPS, and SSA. The impact of ICRS on SGS and SSA are relatively small for SGS smaller than ~300 μm. Ignoring the impact of roughness leads, in general, to a slight overestimation on SGS and an underestimation of SSA. The absolute errors of SGS and SSA introduced by ICRS range from 0.3% - 3%, depending on SGS. Due to the inverse almost linear relationship between SSA and SGS, as presented in Fig. 5, for the same SPS, an overestimation of SGS leads to an underestimation of SSA. The slight overestimation can be found if less ICRS is taken into account in retrieval because the snow reflectance with the same SGS and SPS for ICRS = 0.5 is larger than for ICRS = 0.03 due to lower asymmetry factor of ice crystal with more roughened surface roughness, thus the same surface reflectance observed by satellite requires larger SGS for the case with ICRS = 0.03 used

552 in retrieval in contrast to ICRS = 0.5 used in the forward simulation. However, as can be seen

553 from the right panel of Fig.8, the XBAER algorithm still retrieves the correct SPS ignoring the

554 impact of roughness.
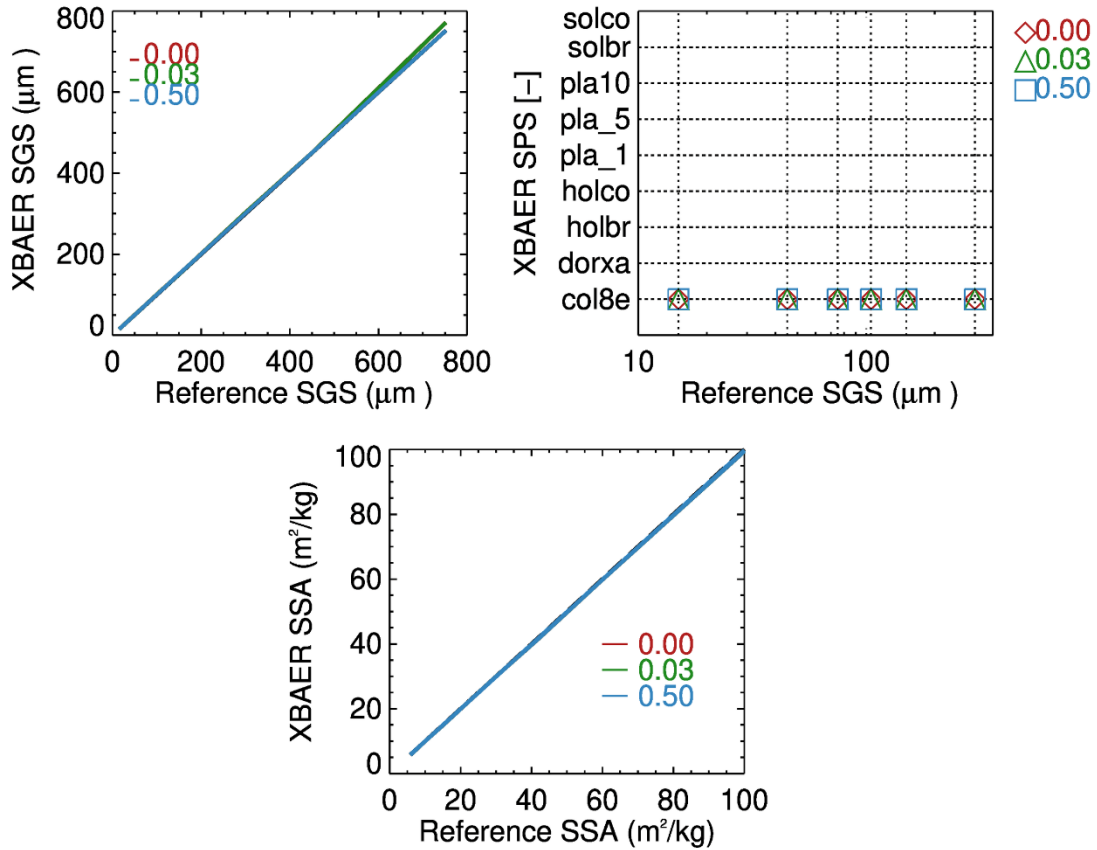
556 Fig 8. Impact of Ice Crystal Surface Roughness (ICSR) on the retrieval of SGS (upper left)

557 SPS (upper right) and SSA (lower). Different colors indicate different ICSR used in the

558 retrieval.

5.4 Impact of aerosol contamination

561 The impact of aerosol on the retrieval of snow properties using passive remote sensing can be

562 important because there is limited aerosol information over the cryosphere (Mei et al., 2013a;

563 Mei et al., 2013b; Mei et al., 2020a; Tomis et al., 2015) to perform an accurate atmospheric

564 correction. The use of MERRA simulated AOT, although with good data quality, will still

565 introduce potential aerosol contamination in the XBAER-derived snow properties. The impact

566 of aerosol on snow properties retrieval is much smaller over Arctic regions compared to middle-

567   low latitude (e.g. Canadian Arctic, Tibetan Plateau) due to large absolute uncertainty in the

568   MERRA simulated aerosol over middle-low latitude in wintertime. A detailed comparison of

569   how possible aerosol contamination may affect the retrieved snow properties will be included

570   in the companion paper (Mei et al., 2020c). In the companion paper, the comparison between

571   satellite-derived and campaign-measured snow properties all over the world will be included.

572   In order to have a better understanding of aerosol contamination on snow properties retrieval,

573   the TOA reflectances were calculated at 0.55 and 1.6 μm with above-given observation

574   geometries using the following settings:

575   ➢   **Snow Layer:** Same as in section 5.1;

576   ➢   **Atmosphere:**

577   ●   Aerosol type is set to be weakly absorbing (Mei et al., 2020b) with AOTs [0.05, 0.08,0.11].

578   Other atmospheric parameters are set according to Bremen 2D Chemical transport model

579   (B2D CTM) for April at 75° N (Sinnhuber et al., 2009). It is worth to notice this three AOT

580   values represent background, average, and pollution conditions in the Arctic as suggested

581   by Mei et al (2020a; 2020b).

582   Fig.9 shows the impact of aerosol contamination on the SGS (upper left), SPS (upper right),

583   and SSA (lower) retrieval. These results are obtained by introducing 50% error in AOT at the

584   step of atmospheric correction and can be considered as the worst case for impact of aerosol

585   contamination on retrieved SGS, SPS, and SSA. The surface reflectances estimated after

586   employing the atmospheric correction were used as components of the vector $\mathbf{A_e}$ in Eq. (1). One

587   can see that aerosol introduces systematic underestimation of retrieved SGS for the given

588   scenarios and the magnitude of underestimation increase with the increase of AOT. For a typical

589   background Arctic aerosol condition, with AOT=0.05, aerosol contamination introduces errors

590   in SGS of less than 3% for SGS ≤150 μm, and less than 7% for 150≤SGS<300 μm. The

591   maximal errors introduced by the aerosol contamination increase to 30% and 37% in the case

592   of average and pollution conditions for AOT=0.08 and 0.11, respectively. Please be noted that

593   the AOT values in the Arctic can be even smaller than 0.05, for instance, AOT over Greenland.

594   Thus, the analysis with respect to aerosol contamination is the worst case for a typical Arctic

595   condition.

596   For the case of AOT = 0.05, SPSs have been correctly retrieved for all SGS values,

597   indicating that under a typical Arctic clean condition, the impact of aerosol is not so large to

598   disturb SPS retrieval. In order to demonstrate the two stages retrieval process and illustrate the

599   impact of aerosol, let us focus on Fig. 10. To facilitate the presentation, we consider the

600   measurement of reflectance at 1.6 μm for a single observation direction (30°) and at 0.55 μm

601   for the difference of reflectance at two observation angles (30° and 55°). This enables avoiding

602   the minimization process given by Eq. (1) and represents the retrieval process in the simple

603   graphic form. The left panel of Fig. 10 depicts the determination of an effective radius for each

604   ice crystal form, assuming the correct shape is aggregate of 8 columns with an effective radius

605   105.4 μm. Solid and dotted lines are surface reflectance of the snow layer consisting of ice

606   crystals with different forms and the dashed line is the measured reflectance after the

607   atmospheric correction. The obtained SGSs are in the range 40 – 120 μm, depending on the

608   selected SPS, and presented in Fig. 10 by solid and dotted vertical lines. In the case of correct

609   SPS selection (aggregate of 8 columns) the retrieved SGS is ~110 μm. The right panel of Fig.

610   10 shows the second stage of the retrieval process, namely, the selection of such SPS for which

611   the difference between measured (dashed line) and simulated value (solid black line) is minimal.

612   In the case under consideration the correct shape is selected with an effective radius ~110 μm.

613   For larger AOT conditions, an inaccurate selection of SPS occurs for all SGS cases,

614   indicating the remaining aerosol information is large enough to decouple the aerosol

615   contribution from the snow surface characteristic. Thus, a quality flag of SPS, associated with

616   AOT, should be introduced in the retrieval of real satellite data. It is interesting to see that "solid

617   bullet rosettes" is the preferable SPS for very strong aerosol contamination cases. This is due

618   to similar scattering properties (shape) of ice crystal and weakly absorbing aerosol, defined in

619   forward simulation. The impact of aerosol contamination, for typical Arctic conditions,

620   introduces less than 5% error in SSA. However, for large aerosol contamination, the around 30%

621   underestimation in SGS linearly introduced about 25% overestimation in SSA, which agrees

622   with the analysis as presented in Fig.7.
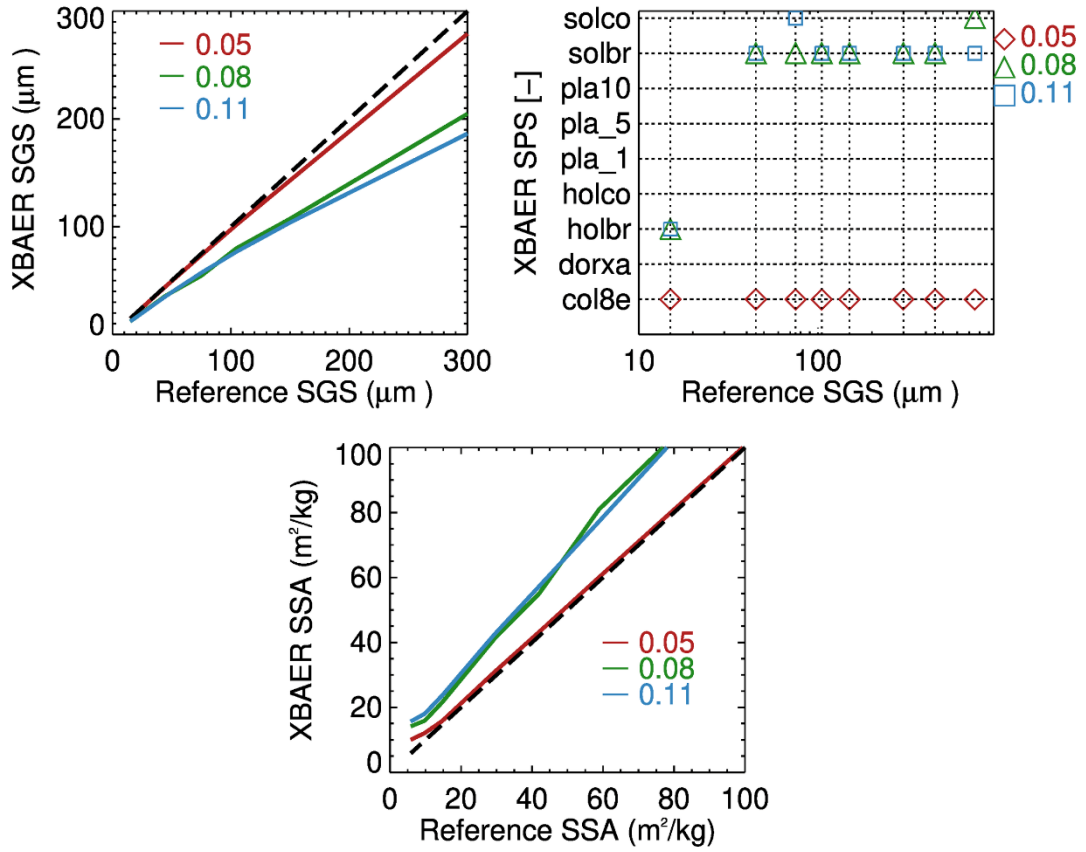
623

624   Fig 9. Impact of aerosol contamination on the retrieval of SGS (upper left) SPS (upper right)

625   and SSA (lower). Different colors indicate different AOT used in forward simulations. No

626   atmospheric correction is performed in the retrieval, black dash line is the 1:1 line.
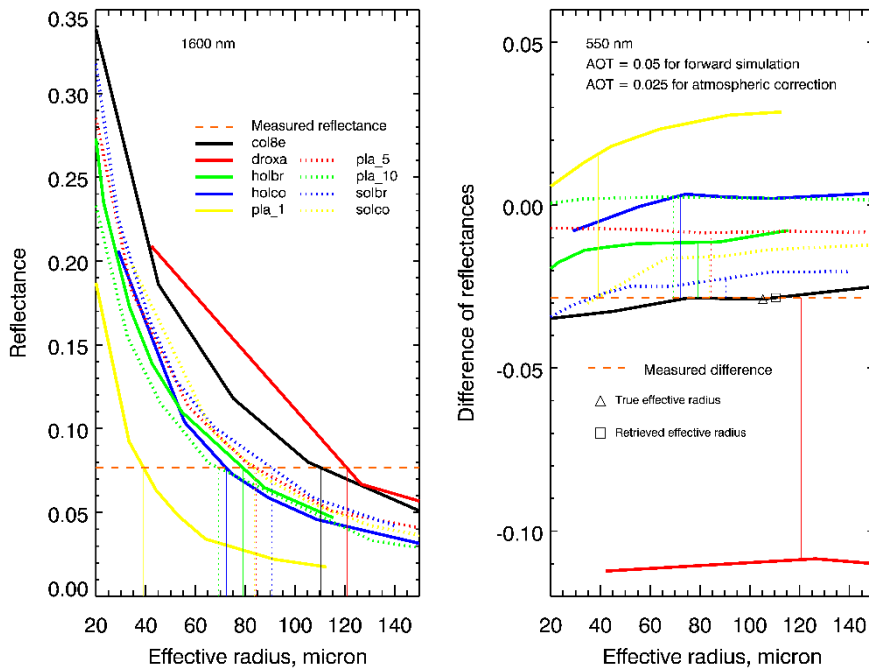
627

628 Fig 10 Schematic representation two stages of the retrieval process. Left panel: determination
629 of effective radius for each ice crystal form. Right panel: selection of optimal SGS, SPS pair.

630

631 **6   Impact of cloud contamination**

632 Any cloud screening method, especially over the cryosphere, may introduce cloud
633 contamination for the retrieval of atmospheric and surface properties (Chen et al., 2014; Mei et
634 al., 2017; Jafariserajehlou et al., 2019). Understanding of the cloud contamination will
635 provide valuable information to interpret the retrieval results using the SLSTR instrument. To
636 investigate the impact of cloud contamination, the following settings were used to perform the
637 simulations of TOA reflectance:

638 ➢ **Snow Layer:** Same as section 5.1;

639 ➢ **Atmosphere:** Aerosol free atmosphere with other parameters as in section 5.4.
640   Additionally, vertically homogeneous ice cloud consisting of aggregate of 8 columns with
641   effective radius of 45 μm and optical thickness [0.1, 0.5, 1.0, 5] is set to be at position of
642   [5 km, 6 km].

643   Fig. 11 shows the impact of cloud contamination on XBAER retrieved SGS (upper left),
644 SPS (upper right), and SSA (lower). The size of ice crystals in ice clouds is typically smaller
645 than snow grain size (Kikuchi et al., 2013). Our statistical analysis of ice crystal effective radius
646 over Greenland shows an average value in the range of 30-50 μm, which is consistent with
647 previous publications (King et al., 2013; Platnick et al., 2017). According to Fig.11, an
648 overestimation of SGS can be found for SGS less than 45μm (cloud effective radius) and an
649 underestimation of SGS for SGS larger than 45μm. The magnitude of
650 overestimation/underestimation increases with the increase of Cloud Optical Thickness (COT).
651 XBAER derived SGS becomes saturated for COT larger than 0.5. Due to limited photon
652 penetration depth for optically thicker clouds (e.g., COT = 5), the XBAER algorithm retrieves
653 the effective radius of ice crystal in the cloud. This demonstrates that theoretically, the XBAER
654 algorithm can retrieve an ice cloud effective radius without a pre-processing of cloud screening.
655 And this can be further used as post-processing to avoid cloud contamination.

656

657   The impact of the cloud on the retrieval of SPS is similar to the impact of aerosol

658   considered above. In short, the cloud plays a larger role for larger SPS (darker TOA) and this

659   impact increases with the increase of COT. However, cloud with large COT can be much easier

660   detected and excluded by the cloud screening algorithm (e.g for the cases with COT > 0.5).

661   SPSs are correctly picked up due to the same SPS used for both the snow layer and the cloud

662   layer. Similar to the impact of aerosol, the underestimation of SGS introduced by the cloud

663   leads to an overestimation of SSA (Fig. 11 (lower panel)). The increase of COT results in

664   saturation of the ice cloud SSA, with a value of 100 m^2/kg in the case of aggregate of 8 columns.

665
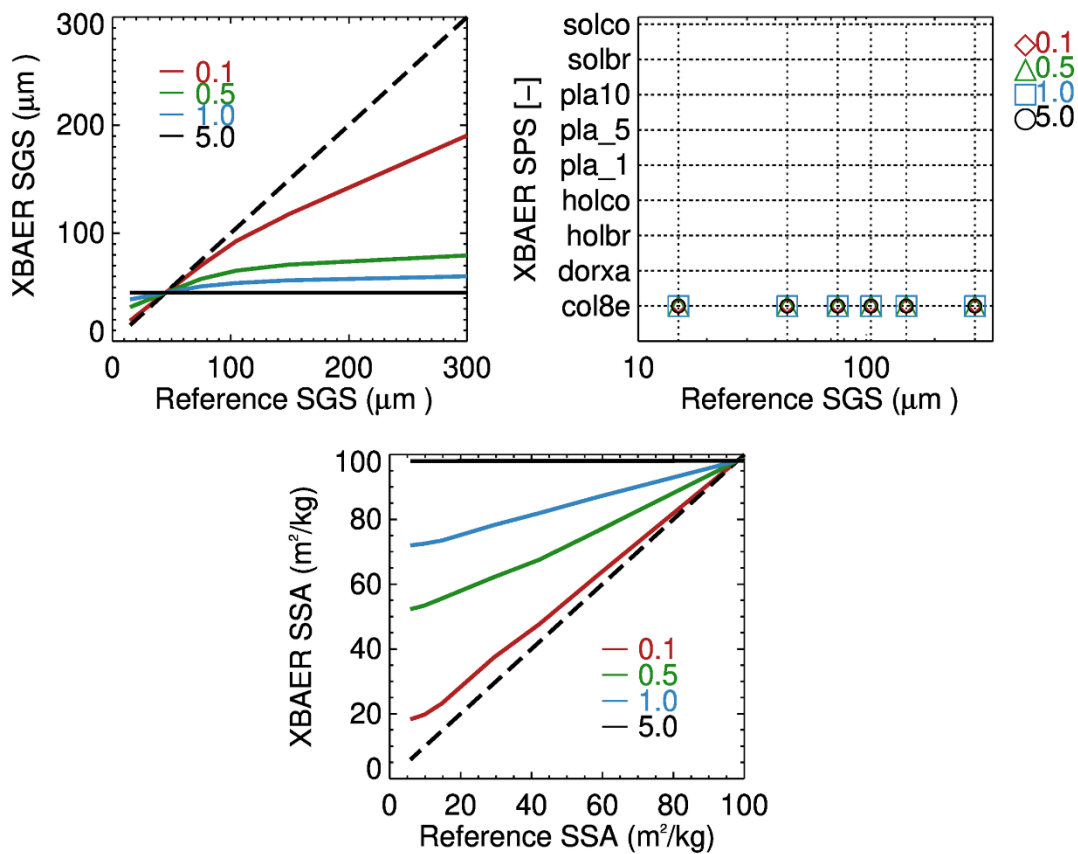
666

667   Fig 11. Impact of cloud contamination on the retrieval of SGS (upper left) SPS (upper right)

668   and SSA (lower). Different colors indicate different COTs in forward simulations, black dash

669   line is the 1:1 line.

670

7   Impact of other factors occurring in reality

The above theoretical investigations include all possible important factors affecting the accuracy XBAER algorithm. However, when applying XBAER algorithm to the SLSTR instrument for real scenarios, two additional factors need to be considered as well. One is the impact of the instrument spectral response function (SRF), the other one is the representativeness of the snow scenario for reality.

7.1 Impact of instrument spectral response function

- ➢ **Snow Layer:** Same as section 5.1;
- ➢ **Atmosphere:** Aerosol free atmosphere with other parameters as in section 5.4.

The forward simulations are performed with and without the impact of Spectral Response Function (SRF). The SRFs for SLSTR at 0.55 and 1.6 μm are shown in Fig. 12. The retrieval is then performed ignoring SRF. Fig. 13 shows the impact of SRF on the retrieval of SGS, SPS, and SSA. For forward simulations without taking SRF into account (labeled as No in Fig. 13), SGS, SPS, and SSA are well received as expected. And it agrees with Fig. 6. However, ignoring the impact of SRF introduces about 7% uncertainties in the simulated surface reflectance and this causes about 5-7% error in both SGS (overestimation) and SSA (underestimation). Taking SRF into account leads to a smaller surface reflectance at 1.6 μm due to potential gas absorption at this wavelength, thus introduces an overestimation for SGS. However, due to a significantly smaller impact at 0.55 μm, the SRF does not play a significant role in the retrieval of SPS.

692
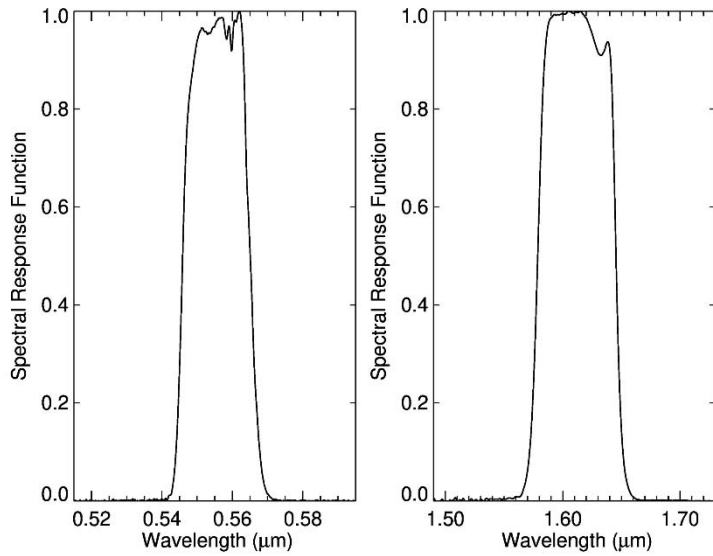
693   Fig. 12 Spectral response function of 0.55 (left) and 1.6 (right) μm of the SLSTR

694   instrument

695
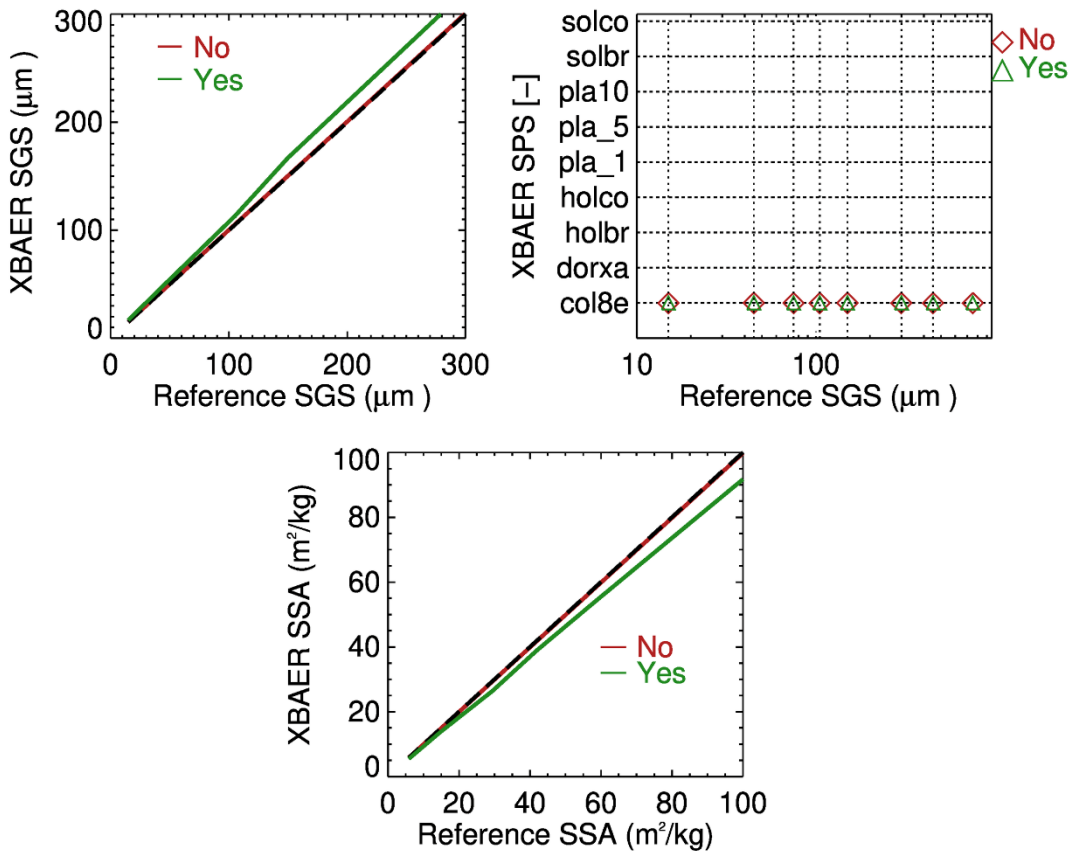
696

697   Fig. 13 Impact of SRFon the retrieval of SGS (upper left) SPS (upper right) and SSA (lower).

698   Different colors indicate retrieval results without (No) and with (Yes) SRF in forward

699   simulations, black dash line is the 1:1 line.

7.2 Impact of snow inhomogeneities

In this section, a realistic model of snow layer is represented by vertically inhomogeneous, polydisperse ice crystals habit mixture. Following Saito et al (2019), the gamma distribution with respect to the maximal dimension will be used to describe polydisperse properties:

$$n(D) = NG(D),$$ (9)

Here, N is the number of ice particles per unit volume, G(D) is the gamma distribution function, i.e.,

$$G(D) = C(D/v)^{k-1}e^{-D/v},$$ (10)

where k and v are the shape and scale parameters, normalization factor C is defined as

$$C = \left[\int_{D_{min}}^{D_{max}} (D/v)^{k-1}e^{-D/v}dD \right]^{-1},$$

(11)

D_{min} and D_{max} describe the minimal and maximum particle sizes in the distribution.

In order to introduce the vertical inhomogeneity, we use the measurement of snow density and equivalent optical diameter vertical profiles conducted during the SnowEx17 campaign. Accounting for that the equivalent optical diameter cannot be directly used to define parameters of Gamma distribution, we use the vertical profile as a shape of the mode (most frequent value in a dataset), i.e.

$$D_0(z) = \frac{D_e(z)}{D_e(z_{top})} D_0(z_{top}),$$ (12)

where $D_e(z)$ is the measured vertical profile of equivalent optical diameter, $D_0(z)$ is the vertical profile of the mode. The mode near the top of snow layer, $D_0(z_{top})$, we assume to be equal 400 μm according to the measurement data reproduced by Saito et al (2019) in Fig. A1.

Taking into account the analytical expression of the mode via shape and scale parameters,

$$D_0 = (k-1)v.$$ (13)

725   and the following relationship between shape and scale parameters derived by Saito et al (2019):

726
$$k = 11.38v^{-0.167} - 2. \tag{14}$$

727   we can estimate parameters k and v of Gamma distribution corrsponding to $D_0(z)$ given by Eq

728   (12).

729   Snow Grain Habit Mixture (SGHM) model is used according to Saito et al (2019). In

730   particular, the particle habits include droxtal, solid hexagonal column, and solid bullet rosette.

731   Habit fraction, $f_h(D)$, as a function of maximal dimension of the SGHM model is presented in

732   the right panel of Fig. 14. The habit fraction is defined so that ,for each D,

733
$$\sum_{h=1}^{3} f_h(D) = 1. \tag{15}$$

734   The selected SGHM model enables us to derive the total volume of ice per unit volume of

735   air as

736
$$V_t = N \sum_{h=1}^{3} \left[\int_{D_{\min}}^{D_{\max}} V_h(D) f_h(D) G(D) dD \right], \tag{16}$$

737   and ice water content (IWC)

738
$$IWC = V_t \rho_{ice}, \tag{17}$$

739   where $V_h(D)$ is the volume of each habit as given in database of Yang and ρ_{ice} is the density of

740   ice.

741   Taking into account that the vettical profile if IWC is measured (see right panel of Fig.

742   13), we can obtain the vertical profile of particle number density. Using Eqs (16) and (17), we

743   have

744
$$N(z) = \frac{IWC(z)}{\rho_{ice} \sum_{h=1}^{3} \left[\int_{D_{\min}}^{D_{\max}} V_h(D) f_h(D) G(D,z) dD \right]}. \tag{18}$$

745   Summing up, we define the microphysical properteis of snow layer using the following

746   model of particle size distribution

$$n(D, z) = N(z)C \left[\frac{(\bar{k}-1)D}{D_0(z)} \right]^{\bar{k}-1} \exp \left[-\frac{(\bar{k}-1)D}{D_0(z)} \right], \qquad (19)$$

where $D_0(z)$ and $N(z)$ are given by Eq (12) and (18), respectively, shape parameter, k, is assumed to be altitude independent and set to 2.3.

The bulk single-scattering properteis of snow layer such as extinction coeffiicent, scattering coefficient and scattering function are defined by the same way as proposed by Baum et al. (2011). For instance, the bulk extinction coefficient is calculated as

$$\beta_{ext}(z) = \int_{D_{min}}^{D_{max}} \left[\sum_{h=1}^{3} \sigma_{ext,h}(D) f_h(D) n(D, z) dD \right], \qquad (20)$$

where $\sigma_{ext,h}(D)$ is the extinction cross-section as given for each habit in database of Yang et al.
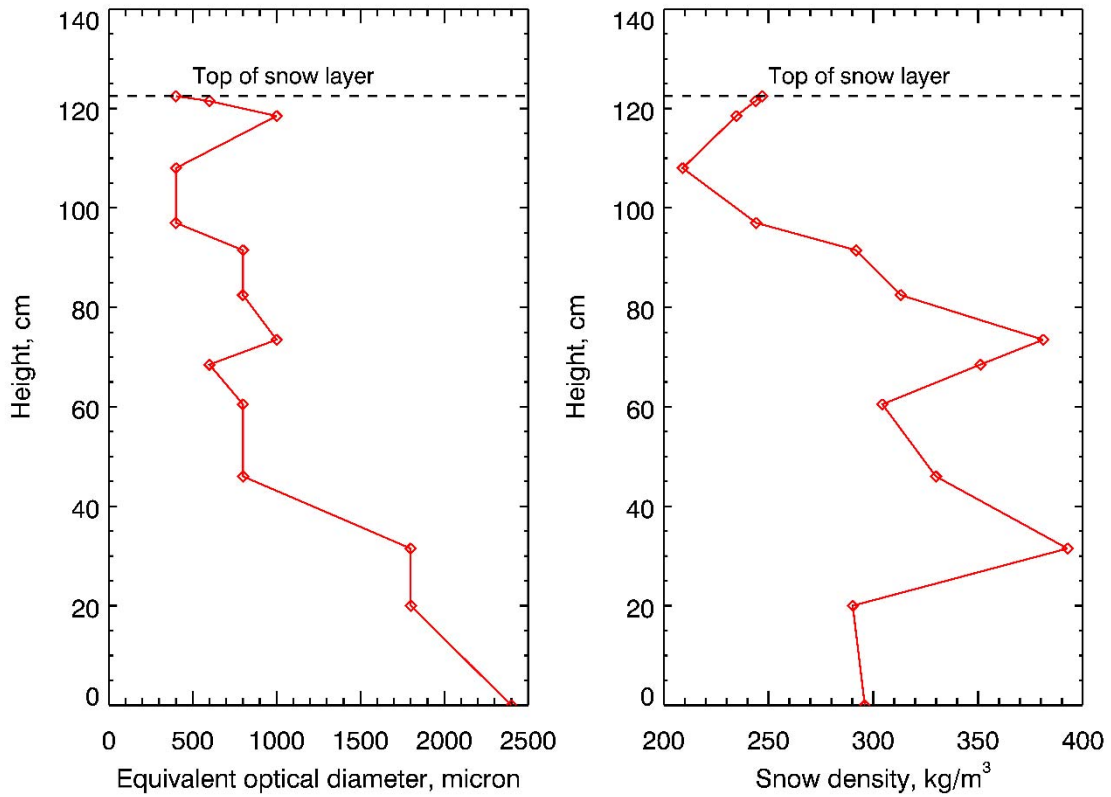
        Fig. 13 Snow properties used for simulations to investigate the impacts of snow layer

    model on XBAER retrieval (left) snow grain size profile and (right) snow density observed

    during SnowEx17 campaign
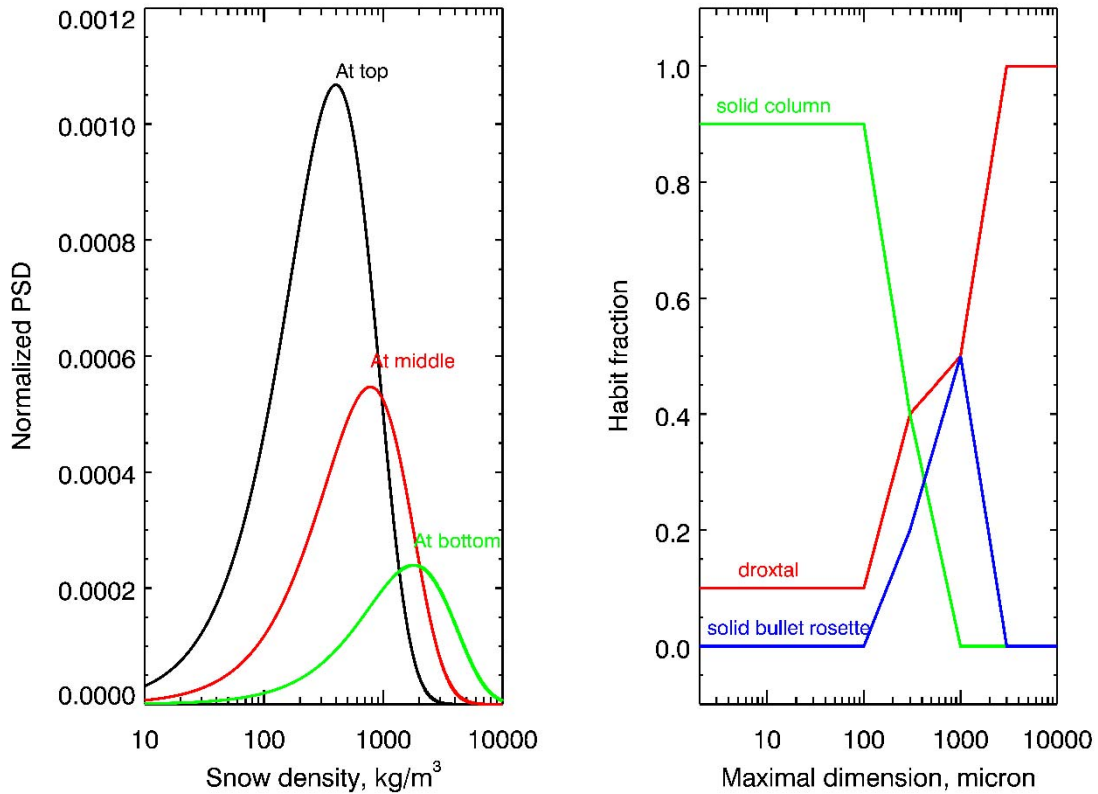
        Fig. 14 Snow properties used for simulations to investigate the impacts of habit mixture

    model on XBAER retrieval: (left) particle size distribution of snow grain size in snow layer;

    (right) habit fraction suggested by Saito et al (2019)

        The following settings are used to simulate the reference snow reflectance at wavelengths

    0.55 and 1.6 μm;

    ➢ **Snow Layer:** vertically inhomogeneous, polydisperse habit mixture and model as

        described above;

    ➢ **Atmosphere:** excluded.

        Using the simulated reflectances in XBAER algorithm, we have retrieved SPS as dorxtal

    with the maximal dimension equal to 740 μm. Taking into account that the model of PSD near

    the top of snow layer is 400 μm and the mean value calculated as $kD_0/(k-1)$ is equal to 708 μm,

773   one can see that the retrieved maximal dimension is an estimation of mean value of PSD near

774   the top of snow layer.

775   Since there is no single reference SGS values when a PSD is used, it is important to check

776   the representativeness of XBAER derived SGS. Accounting for that the mode and mean values

777   for a given PSD are two typical "effective" way to describe polydisperse medium, we compared

778   reflectances of snow layer calculated assuming PSD in the form of Gamma distribution and

779   assuming monodisperse medium with SGS equal to the mode or to the mean of selected PSD.

780   In order to simplify analysis, we consider vertically homogeneous snow layer consisting of only

781   single particle habit. The calculations of reflectance were performed for severely roughened

782   aggregate of 8 columns and droxtal particles setting the shape parameter, k, equal to 2.3 and

783   the model equal to [100, 300, 500, 700, 1000, 2000, 3000, 5000] μm.

784   Fig. 15 shows the comparison of snow reflectance calculated assuming monodisperse and

785   polydisperse snow model. In the case of monodisperse model, SGS is assumed to be equal to

786   the mean or to the mode value of PSD. We can see that the surface reflectance calculated using

787   the mean value of PSD agrees better with reference values, tan reflectance calculated using the

788   mode value. In particular, the root-mean-square deviation (RMSE) values are more than 2 times

789   smaller. One can also see from Fig. 15 that the difference between monodisperse reflectances

790   calculated using mean or mode PSD values decreases with increase of the PSD mode. It can be

791   explained due to the fact that the increase of PSD mode leads to the increase of absorption and

792   decrease of reflectance sensitivity with respect to the variation of SGS.
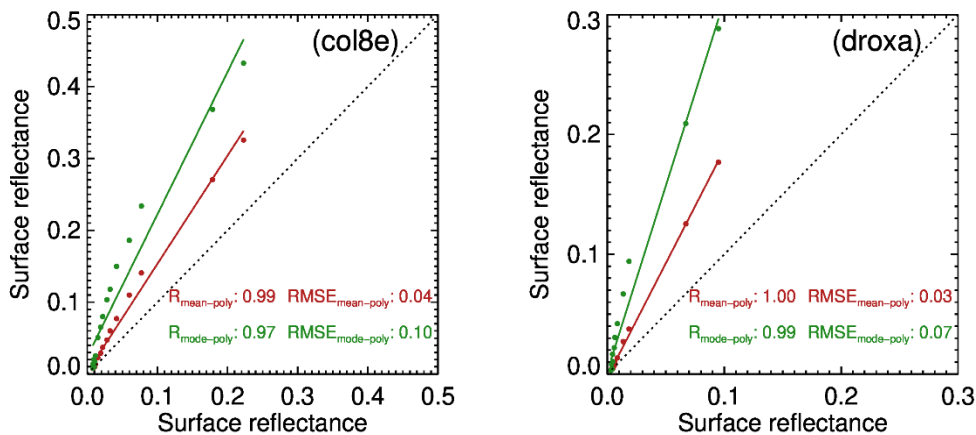
793

794 Fig. 15 The comparison between simulated snow reflectance using mono and poly-disperse

795 snow model consisting of aggregate of columns (left) and droxtal (right). In the case of

796 monodisperse model, the SGS is assumed to be the mean and mode value of PSD at the top of

797 snow layer (see left panel of Fig. 14). The reference value is shown on the x-axis.

798

8 Conclusions

800 SGS, SPS, and SSA are three important parameters to describe snow properties. They play

801 important roles in the changes in snow albedo/reflectance and impact the atmospheric and

802 energy-exchange processes. A better knowledge of SGS, SPS, and SSA can provide more

803 accurate information to describe the impact of snow on Arctic amplification processes. The

804 information about SGS, SPS, and SSA may also explore new applications to understand the

805 atmospheric conditions (e.g. aerosol loading). Although some previous attempts (e.g. Lyapustin

806 et al., 2009) show the capabilities of using passive remote sensing to derive SGS over a large

807 scale, no publication has been found to derive SGS, SPS, and SSA simultaneously. To our best

808 knowledge, this is the first paper, attempting to retrieve these parameters using satellite

809 observations.

810 The new algorithm is designed within the framework of the XBAER algorithm. The

811 XBAER algorithm has been applied to derive SGS, SPS, and SSA using the newly launched

812 SLSTR instrument onboard Sentinel-3 satellite. This is the first part of the paper, to describe

813 the algorithm, and to present the sensitivity studies.

814 The SGS, SPS, and SSA retrieval algorithm is based on the recent publication by Yang et

815 al., (2013), in which a database of optical properties for nine typical SPSs (aggregate of 8

816 columns, droxtal, hollow bullet rosettes, hollow column, plate, aggregate of 5 plates, aggregate

817 of 10 plates, solid bullet rosettes, column) are provided. Previous publications show that this

818 database can be used to retrieve ice crystal properties in both ice cloud and snow (e.g., Järvinen

819 et al., 2018; Saito et al., 2019). The algorithm is a LUT-based approach, in which the

820 minimization is achieved by the comparison between atmospherically corrected TOA

821 reflectance at 0.55 and 1.6 μm observed by SLSTR and pre-calculated LUT of surface

822   reflectances under different geometries and snow properties. The retrieval is relatively time-

823   consuming because the minimization has to be performed for each SPS and the optimal SGS

824   and SPS are selected after 9 minimizations are done. The SSA is then obtained using the

825   retrieved SGS and SPS based on another pre-calculated LUT.

826   The sensitivity studies with respect to the impacts of SPS, ICSR, aerosol and cloud

827   contamination on XBAER derived SGS and SPS provide a comprehensive understanding of

828   the retrieval accuracy of the new algorithm. The main findings of the theoretical considerations

829   are: (1) XBAER derived SGS is more likely to represent the average SGS near the top of snow

830   layer when a PSD is known; (2) SPS plays an important role for the retrieval accuracy of SGS,

831   the retrieved SGS can differ several times by usage different SPSs in the retrieval process; (3)

832   Impact of ICSR on the retrieval accuracy of SGS can be neglected, ignoring ICSR completely

833   may introduce maximal 3% error on the retrieval accuracy of SGS, especially for large ice

834   crystals; (4) Assumption of convex particle shape (e.g., sphere) of a non-convex ice crystal

835   leads to the underestimation of the retrieved SSA; (5) The impact of aerosol and cloud increase

836   with the increase of both aerosol/cloud loading and SGS; (6) The impact of instrument SRF

837   may introduce some positive biase for SGS and negative bias for SSA, however, it plays no

838   role for the determination of SPS

839   Even though all major possible factors affecting the retrieval accuracy of XBAER

840   algorithm are investigated in this paper, in reality, the final retrieval accuracy can only be

841   evaluated by performing a thorough comparison with independent measurement results because

842   uncertainties caused by each individual factor can compensate each other in the real satellite

843   retrieval. All details of such validation can be found in the companion paper of Mei et al (2020c).

Acknowledgements

845   This research was funded by the Deutsche Forschungsgemeinschaft (DFG, German Research

846   Foundation) – Project-ID 268020496 – TRR 172. The SLSTR data is provided by ESA. We

847   thank the valuable discussion with Dr. M Saito.

848

849

850

Appendix

852 According to the definition of specific surface area

$$SSA = \frac{A}{\rho V}, \tag{A1}$$

854 one needs to calculate the total area A of ice crystal. In the following sections, we consider

855 in details the basic equations to calculate total area and SSA of different SPSs given in

856 database of Yang et al (2013) and used above within the retrieval algorithm.

857

858 ➢ **Droxtal, solid column, plate**

859 In the case of convex faceted particles such as droxtal, solid column, and plate, the

860 calculation of total area is straightforward and based on the Cauchy's surface area formula:

$$A = 4A_p. \tag{A2}$$

862 Taking into account that for selected SPS, one can find corresponding V and A_p in database

863 given by Yang et al., (2013), we have the following results for SSA of such particles:

$$SSA = \frac{4A_p}{\rho V}. \tag{A3}$$

865 ➢ **Hollow column**

866 In this case a solid column includes two equal cavities in the form of a hexagonal

867 pyramid and cannot be considered as convex particle. The aspect ratio of hollow column

868 with the height, d, of hexagonal pyramid is given according to Yang et al., (2013) as:

$$\frac{2a}{L} = \begin{cases} 0.7, & L < 100\,\mu m \\ \dfrac{6.96}{\sqrt{L}}, & L \geq 100\,\mu m \end{cases}, \quad d = 0.25L. \tag{A4}$$

870 The volume of such hollow column is given by

871
$$V = V_c - 2V_p,$$
(A5)

872   where the volume of solid column, V_c, and a hexagonal pyramid, V_p, are,

873
$$V_c = \frac{3\sqrt{3}}{2}a^2 L,$$
(A6)

874
$$V_p = \frac{\sqrt{3}}{2}a^2 d.$$
(A7)

875   Thus, the volume, V, is

876
$$V = \frac{\sqrt{3}}{2}a^2(3L - 2d).$$
(A8)

877   Employing the relationship between d and L given by Eq (A4) and excluding a, we
878   have

879
$$V = \frac{2.5\sqrt{3}}{2}a^2 L \begin{cases} m_0 m_1^2 L^3, & L < 100\mu m \\ m_0 m_2^2 L^2, & L \geq 100\mu m \end{cases},$$
(A9)

880   where $m = \dfrac{2.5}{\sqrt{3}/2}, m_1 = \dfrac{0.7}{2}$, and $m = \dfrac{6.96}{2}$. For a selected volume, V, the length,

881   L, is calculated as follows:

882
$$L = \begin{cases} [V/m_0/m_1^2]^{\frac{1}{3}}, & V < V_{100} \\ [V/m_0/m_2^2]^{\frac{1}{2}}, & V \geq V_{100} \end{cases},$$
(A10)

883   where $V_{100} = m_0 m_2^2 100^2.$

884   Let us now calculate the area of each triangle side of the pyramid

885    $S_t = \dfrac{a}{2}\sqrt{d^2 + \dfrac{3a^2}{4}}.$
(A11)

886   The area of lateral surface of two pyramids is

887       $$S_p = 3a\sqrt{4d^2 + 3a^2}.$$

888   (A12)

889   And the total surface area of hollow column is given by

890    $$S = 6aL + 3a\sqrt{4d^2 + 3a^2},$$ (A13)

891   where a and d should be expressed via L according to Eq. (A4).

892   Having obtained the total area, one can calculate specific surface area

893    $$SSA = \frac{S}{\rho V},$$ (A14)

894   ➢ **Hollow bullet rosettes**

895   In this case a solid column includes a cavity in the form of a hexagonal pyramid with

896 height H and a hexagonal pyramid with height t on the opposite site of column. The aspect

897 ratio and parameters H and t is given according to Yang et al., (2013) as:

898    $$\frac{2a}{L} = 2.3104 L^{-0.37}, \quad t = \frac{\sqrt{3}a}{2\tan(28^\circ)}, \quad H = 0.5(t + L).$$ (A15)

899   The volume of a hollow bullet rosettes is given by

900    $$V_1 = V_c - V_- + V_+.$$ (A16)

901   Using Eq. (A16), we have

902    $$V_1 = \frac{3\sqrt{3}}{2}a^2 L - \frac{\sqrt{3}}{2}a^2 H + \frac{\sqrt{3}}{2}a^2 t = \frac{\sqrt{3}}{2}a^2(3L - H + t).$$ (A17)

903   Substituting H as given by Eq (A15), we obtain

904 $$V_1 = \frac{\sqrt{3}a^2}{4}(5L+t).$$ (A18)

905 Using formula given by Eq (A15), we express parameters a and t of hollow bullet
906 rosettes via L:

907 $$a = m_a L^{p_a},$$ (A19)

908 $$t = m_t m_a L^{p_a},$$ (A20)

909 where coefficients, m_a, m_t, and p_a are

910 $$m_a = \frac{2.3104}{2}, m_t = \frac{\sqrt{3}}{2\tan(28°)}, p_a = 1-0.37.$$

911 (A21)

912 The expression (A18) can be rewritten as:

913 $$V_1 = \frac{3}{4}m_a^2 L^{2p_a+1}(5+m_t m_a L^{-0.37}).$$ (A22)

914 For a desired volume V of hollow bullet rosettes, consisting of 6 equal rosettes
915 (See Table 1), this equation was solved with respect to the length, L, of the hollow bullet
916 rosette using following iterative process:

917 $$L_n = [\frac{2V}{3\sqrt{3}m_a^2(5+m_t m_a L_{n-1}^{-0.37})}]^{\frac{1}{2p_a+1}}.$$ (A23)

918 The iterative process starts with $L_0=1$ and finishes when $\left|\frac{L_n-L_{n-1}}{L_n}\right| \leq 10^{-4}$. The total

919 area of hollow bullet rosettes is calculated as;

920 $$S_1 = 6aL + \frac{3a}{2}\sqrt{4H^2+3a^2} + \frac{3a}{2}\sqrt{4t^2+3a^2}.$$ (A24)

921 The SSA is given by

922
$$SSA = \frac{6S_1}{\rho V}.$$
(A25)

➢ **Solid bullet rosettes**

924   The aspect ratio and parameter t are given according to Yang et al., (2013) as:

925
$$\frac{2a}{L} = 2.3104 L^{-0.37}, \quad t = \frac{\sqrt{3}a}{2\tan(28^\circ)}.$$
(A26)

926   The volume of single solid bullet rosette is

927
$$V_1 = V_c + V_+.$$
(A27)

928   Using Eq. (A6), we have

929
$$V_1 = \frac{3\sqrt{3}}{2} a^2 L + \frac{\sqrt{3}}{2} a^2 t = \frac{\sqrt{3}}{2} a^2 (3L + t).$$
(A28)

930   Using formula given by Eq (A26), we express parameters a and t of solid bullet rosette
931   via L:

932
$$a = m_a L^{p_a},$$
(A29)

933
$$t = m_t m_a L^{p_a},$$
(A30)

934   Where coefficients, m_a, m_t, and p_a are the same as in the case of hollow bullet
935   rosette given bu Eq. (A21). The expression Eq. (A28) can be rewritten as

936
$$V_1 = \frac{3}{2} m_a^2 L^{2p_a + 1} (3 + m_t m_a L^{-0.37}).$$
(A31)

937   For a desired volume V of solid bullet rosettes, consisting of 6 equal rosettes (see
938   Table 1), this equation was solved with respect to the length, L, of the solid bullet rosette
939   using following iterative approach:

940
$$L_n = [\frac{V}{3\sqrt{3}m_a^2(3+m_t m_a L_{n-1}^{-0.37})}]^{\frac{1}{2p_a+1}}.$$
(A32)

941   The total area of solid bullet rosettes is calculated as;

942
$$S_1 = 6aL + \frac{3\sqrt{3}a^2}{2} + \frac{3a}{2}\sqrt{4t^2+3a^2}.$$
(A33)

943   The SSA is given by

944
$$SSA = \frac{6S_1}{\rho V}.$$
(A34)

945

946   ➢ **Aggregate of 5 and 10 plates**

947   According to the paper of Yang et al (2013), Table 1 provides the aspect ratios of the

948 ice crystal habits. In the case of an aggregate of columns or plates, the semi-width a and

949 length L of each hexagonal element of the aggregate are on a relative scale. In order to covert

950 these parameters in absolute values, let us consider the following relationship given in Yang

951 et al (2013) for aspect ratio of plate:

952
$$\frac{2a}{L} = \begin{cases} 1, & a \le 2\mu m \\ m_1 a + m_0, & 2 < a < 5\mu m \\ ma^p, & a \ge 5\mu m \end{cases}$$
(A35)

953   where constants are: m_1=0.2914, m_0=0.4172, m=0.8038, p=0.526.

954   Using this expression and accounting for that relative values for a, given in Table 1, are

955 greater than 5μm, we can express L_r via a_r as

956
$$L_r = \frac{2a_r}{ma_r^p} = \frac{2a_r^{1-p}}{m}.$$
(A36)

957 where subscript r denotes that they are on relative scale. The volume of a hexagonal plate on
958 relative scale is given by

959
$$v_r = \frac{3\sqrt{3}}{2} a_r^2 L_r = \frac{3\sqrt{3}}{m} a_r^{3-p}.$$
(A37)

960 The volume of aggregates of 5 or 10 plates is given by

961
$$V_r = \frac{3\sqrt{3}}{m} \sum_{i=1}^{N} a_{r,i}^{3-p},$$
(A38)

962 where $N=5$ and $N=10$ for 5 and 10 plates, respectively. The absolute value of the volume,

963 V, for a selected maximal dimension of aggregate of 5 or 10 plates one can find in database

964 presented by Yang et al (2013). Introducing the scaling factor

965
$$C = \frac{V_r}{V},$$
(A39)

966 We rewrite expression (A38) as

967
$$C = \frac{V_r}{C} = \frac{3\sqrt{3}}{mC} \sum_{i=1}^{N} a_{r,i}^{3-p} = \frac{3\sqrt{3}}{m} \sum_{i=1}^{N} a_i^{3-p},$$
(A40)

968 where the absolute value of semi-width, a_i, is given by

969
$$a_i = \frac{a_{r,i}}{C^{(3-p)^{-1}}},$$
(A41)

970 Having obtained the absolute value of a_i for each plate, the length L_i is calculated as:

971
$$L_i = \begin{cases} 2a_i, & a \le 2\mu m \\ \dfrac{2a_i}{m_1 a_i + m_0}, & 2 < a < 5\mu m \\ \dfrac{2}{m_1 a^{(1-p)}}, & a \ge 5\mu m \end{cases}$$
(A42)

972

973 The total area of a hexagonal plate with semi-width a_i and length L_i is given by

974
$$S_i = 2\frac{3\sqrt{3}}{2} a_i^2 + 6a_i L_i,$$
(A43)

975 The total area is given by

976
$$S = \sum_{i=1}^{N} S_i.$$
(A44)

977 Having obtained the total area, one can calculate SSA as the total surface area of a material per
978 unit of mass:

979
$$SSA = \frac{S}{\rho V},$$
(A45)

980   where ρ=917 kg/m^3 is the density of ice.

981

982

983

984

985

986

987 **Reference**

988   Aoki, T., Fukabori, M., Hachikubo, A., Tachibana, Y., and Nishio, F.: Effects of snow physical parameters on

989   spectral albedo and bidirectional reflectance of snow surface, *J. Geophys. Res.*, 105(D), 10 219–10 236, 2000.

990   Baker, I.: Microstructural characterization of snow, firn and ice, *Philosophical Transactions of the Royal Society a-*

991   *Mathematical Physical and Engineering Sciences*, 377, 10.1098/rsta.2018.0162, 2019.

992   Battaglia, A., Rustemeier, E., Tokay, A., Blahak, U., and Simmer, C.: PARSIVEL snow observations: a critical

993   assessment, *J. Atmos. Ocean. Tech.*, 27, 333–344, doi:10.1175/2009JTECHA1332.1, 2010.

994   Baum, B. A., P. Yang, A. J. Heymsfield, C. Schmitt, Y. Xie, A. Bansemer, Y. X. Hu, and Z. Zhang, Improvements

995   to shortwave bulk scattering and absorption models for the remote sensing of ice clouds. *J. Appl. Meteor. Clim.*, 50,

996   1037-1056, 2011

997   Cauchy, A.: Note sur divers th́eor̀ems relatifs `a la rectification des courbes et `a la quadrature des surfaces. C.R.

998   Acad. Sci., 13:1060–1065, 1841.

999   Chen, N., W. Li, T. Tanikawa, M. Hori, T. Aoki, and K. Stamnes: Cloud mask over snow/ice covered areas for the

1000   GCOM-C1/SGLI cryosphere mission: Validations over Greenland, J. Geophys. Res. Atmos., 119, 12,287-12,300,

1001   doi: 10.1002/2014JD022017, 2014.Colbeck, S. C.: Thermodynamics of snow metamorphism due to variations in

1002   curvature, J. Glaciol., 26, 291-301, 10.3189/S0022143000010832, 1980.

1003   Colbeck, S. C.: Theory of metamorphism of dry snow, J. Geophys. Res., 88, 5475-5482, 1983.

1004   Cole, B. H., Yang, P., Baum, B. A., Riedi, J., and C.-Labonnote, L.: Ice particle habit and surface roughness derived

1005   from PARASOL polarization measurements, *Atmos. Chem. Phys.*, 14, 3739-3750, https://doi.org/10.5194/acp-14-

1006   3739-2014, 2014.

1007   Cox, S. C., and Munk, W. H. : Measurement of the roughness of the sea surface from photographs of the sun's glitter.

1008   *J. Opt. Soc. Amer.*, 44, 838–850, 1954.

1009   Dietz, A.J., Kuenzer, C., Gessner, U. and Dech, S. : Remote sensing of snow – a review of available methods,

1010   *International Journal of Remote Sensing*, 33:13, 4094-4134, DOI: 10.1080/01431161.2011.640964, 2012.

1011   Domine, F., Gallet, J. C., Barret, M., Houdier, S., Voisin, D., Douglas, T., Blum, J. D., Beine, H., and Anastasio, C.:

1012   The specific surface area and chemical composition of diamond dust near Barrow, Alaska, *J. Geophys. Res.*, 116,

1013   D00R06, 10.1029/2011JD016162 2011.

1014   Domine, F., Picard, G., Morin, S., Barrere, M., Madore, J. B., and Langlois, A.: Major Issues in Simulating Some

1015   Arctic Snowpack Properties Using Current Detailed Snow Physics Models: Consequences for the Thermal Regime

1016   and Water Budget of Permafrost. *Journal of Advances in Modeling Earth Systems.* 11(1), 34-44,

1017   https://doi.org/10.1029/2018MS001445,2019

1018   Donahue, C. , Skiles, S.M. and Hammonds, K.: In situ effective snow grain size mapping using a compact

1019   hyperspectral imager. *Journal of Glaciology,* 1–9. https://doi.org/10.1017/jog.2020.68,2020.

1020   Dumont, M., Brissaud, O., Picard, G., Schmitt, B., Gallet, J.-C., and Arnaud, Y.: High-accuracy measurements of

1021   snow Bidirectional Reflectance Distribution Function at visible and NIR wavelengths – comparison with modelling

1022   results, *Atmos. Chem. Phys.*, 10, 2507-2520, https://doi.org/10.5194/acp-10-2507-2010, 2010.

1023   Flanner, M. G. and Zender, C. S.: Linking snowpack microphysics and albedo evolution, *J. Geophys. Res.*, 111,

1024   D12208, doi:10.1029/2005JD006834, 2006.

1025   Frei, A., Tedesco, M., Lee, S., Foster, J., Hall, D. K., Kelly, R., and Robinson, D. A.: A review of global satellite-

1026   derived snow products, Adv. Space Res., Oceanography, Cryosphere and Freshwater Flux to the Ocean, 50, 1007–

1027   1029, 2012.

1028   Gallet, J.-C., Domine, F., Zender, C. S., and Picard, G.: Measurement of the specific surface area of snow using

1029   infrared reflectance in an integrating sphere at 1310 and 1550 nm, *The Cryosphere*, 3, 167-182, 2009.

1030   Gardner, A.S. and Sharp, M.J: A review of snow and ice albedo and the development of a new physically based

1031   broadband albedo parameterization, *Journal of Geophysical Research*, 115, F01009, doi:10.1029/2009JF001444,

1032   2010Gordon, M. and Taylor, P. A.: The Electric Field During Blowing Snow Events, *Bound-lay. Meteorol.*, 130,

1033   97–115, 2010.

1034   Grenfell, T.C. and Warren, S.G. : Representation of a nonspherical ice particle by a collection of independent spheres

1035   for   scattering   and   absorption   of   radiation.   *J.   Geophys.   Res.*   104   (D24),   31697–31709.

1036   http://dx.doi.org/10.1029/1999JD900496,1999

1037   Hagenmuller, P., Matzl, M., Chambon, G., and Schneebeli, M.: Sensitivity of snow density and specific surface area

1038   measured by microtomography to different image processing algorithms, *The Cryosphere*, 10, 1039–1054,

1039   https://doi.org/10.5194/tc-10-1039-2016, 2016.

1040   Hansen, J. and Nazarenko, L.: Soot climate forcing via snow and ice albedos, *Proc. Nat. Acad. Sci.*, 101, 423–428,

1041   2004

1042   Jafariserajehlou, S., Mei, L., Vountas, M., Rozanov, V., Burrows, J. P., and Hollmann, R.: A cloud identification

1043   algorithm over the Arctic for use with AATSR–SLSTR measurements, Atmos. Meas. Tech., 12, 1059–1076,

1044   https://doi.org/10.5194/amt-12-1059-2019, 2019.

1045   Järvinen, E., Jourdan, O., Neubauer, D., Yao, B., Liu, C., Andreae, M. O., Lohmann, U., Wendisch, M., McFarquhar,

1046   G. M., Leisner, T., and Schnaiter, M.: Additional global climate cooling by clouds due to ice crystal complexity,

1047   *Atmos. Chem. Phys.*, 18, 15767–15781, https://doi.org/10.5194/acp-18-15767-2018, 2018.

1048   Jiao, Z., A. Ding, A. Kokhanovsky, C. Schaaf, F. Bréon, Y. Dong, Z. Wang, Y. Liu, X. Zhang, S. Yin, L. Cui, L.

1049   Mei, Y. Chang: Development of a Snow Kernel to Better Model the Anisotropic Reflectance of Pure Snow into a

1050   Kernel-Driven   BRDF   Model   Framework, *Remote   Sensing   Environment*, 221,   198-

1051   209, doi:10.1016/j.rse.2018.11.001, 2019.

1052   Jin, Z., Charlock, T. P., Yang, P., Xie, Y., and Miller, W. : Snow optical properties for different particle shapes with

1053   application to snow grain size retrieval and MODIS/CERES radiance comparison over Antarctica. *Remote Sensing*

1054   *of Environment*, 112(9), 3563–3581. doi:10.1016/j.rse.2008.04.011,2008

1055   Kikuchi, K., Kameda, T., Higuchi, K., and Yamashita, A.: A global classification of snow crystals, ice crystals, and

1056   solid precipitation based on observations from middle latitudes to polar regions, *Atmos. Res.*, 132-133, 460–472,

1057   2013.

1058   King, M.D., Platnick, S., Menzel, W.P., Ackerman, S.A., Hubanks, P.A.: Spatial and temporal distribution of clouds

1059   observed by MODIS onboard the Terra and Aqua satellites, *IEEE Trans. Geosci. Remote Sens.* 51 (7), 3826–3852,

1060   2013.

1061   Kokhanovsky, A., Lamare, M.; Danne, O., Brockmann, C., Dumont, M., Picard, G., Arnaud, L., Favier, V., Jourdain,

1062   B.; Le Meur, E., Di Mauro, B., Aoki, T., Niwano, M., Rozanov, V., Korkin, S., Kipfstuhl, S., Freitag, J., Hoerhold,

1063   M., Zuhr, A., Vladimirova, D., Faber, A.-K., Steen-Larsen, H.C., Wahl, S., Andersen, J.K., Vandecrux, B., van As,

1064   D., Mankoff, K.D., Kern, M., Zege, E., Box, J.E.: Retrieval of Snow Properties from the Sentinel-3 Ocean and Land

1065   Colour Instrument, *Remote Sens.*, 11, 2280, 2019.

1066   Konig, M., Winther, J.-G. and Isaksson, E.: Measuring snow and glacier ice properties from satelllite, *Reviews of*

1067   *Geophysics*, 39, 1-27, 2001.

1068   Koren, H., Snow grain size from satellite images, SAMBA/31/09, publications.nr.no/5119/Koren_-

1069   _Snow_grain_size_from_satellite_images.pdf, 2009 (last acess:7 May, 2018)

1070   Kukla G., Barry, R.G., Hecht, A., Wiesnet, D. eds (1986) SNOW WATCH'85. Proceedings of the workshop held

1071   28-30 October 1985 at the University of Maryland, College Park, MD> Boulder, Colorado, Word Data Center A for

1072   Glaciology (Snow and Ice), *Glaciological Data*, Report GD-18, P 215-223, 1986

1073   Langlois, A., Royer, A., Montpetit, B., Roy, A., and Durocher, M.: Presenting Snow Grain Size and Shape

1074   Distributions in Northern Canada Using a New Photographic Device Allowing 2D and 3D Representation of Snow

1075   Grains. *Frontiers in Earth Science*, 7. doi:10.3389/feart.2019.00347,2020

1076   Legagneux, L. and Domine, F.: A mean field model of the decrease of the specific surface area of dry snow during

1077   isothermal metamorphism, J. Geophys. Res., 110, F04011, https://doi.org/10.1029/2004JF000181, 2005.

1078   Legagneux, L., Cabanes, A., and Domine, F.: Measurement of the specific surface area of 176 snow samples using

1079   methane adsorption at 77 K, J. Geophys. Res., 107, 4335, 10.1029/2001jd001016, 2002.

1080   Leroux C., and Fily M. : Modeling the effect of sastrugi on snow reflectance, *J. Geophys. Res.*, 103, 25,779-

1081   25,788, 1998.

1082   Li, W., Stamnes, K., Chen, B., and Xiong, X.: Snow grain size retrieved from near-infrared radiances at multiple

1083   wavelengths, *Geophys. Res. Lett.*, 28, 1699–1702, doi:10.1029/2000GL011641, 2001.

1084   Libois, Q., Picard, G., France, J. L., Arnaud, L., Dumont, M., Carmagnola, C. M., and King, M. D.: Influence of

1085   grain shape on light penetration in snow, *The Cryosphere*, 7, 1803–1818, https://doi.org/10.5194/tc-7-1803-2013,

1086   2013.

1087   Liu, J. P., Judith, A. C., Wang, H. J., Song, M. R., and Radley, M. H.: Impact of declining Arctic sea ice on winter

1088   snowfall, *P. Natl. Acad. Sci.*, doi:10.1073/pnas.1114910109, 2012.

1089   Livneh, B., Xia, Y., Mitchell, K. E., Ek, M. B., and Lettenmaier, D. P.: Noah LSM snow model diagnostics and

1090   enhancements, *J. Hydrometeorol.*, 11, 721–738, 2009.

1091   Lyapustin, A., Tedesco, M., Wang, Y.J., Aoki, T., Hori, M. and Kokhanovsky, A. : Retrieval of snow grain size over

1092   Greenland from MODIS, *Remote Sensing of Environment*, 113, 1976-1987,2009.

1093   Mary, A., Dumont, M., Dedieu, J.-P., Durand, Y., Sirguey, P., Milhem, H., Mestre, O., Negi, H. S., Kokhanovsky,

1094   A. A., Lafaysse, M., and Morin, S.: Intercomparison of retrieval algorithms for the specific surface area of snow

1095   from near-infrared satellite data in mountainous terrain, and comparison with the output of a semi-distributed

1096   snowpack model, *The Cryosphere*, 7, 741–761, https://doi.org/10.5194/tc-7-741-2013, 2013.

1097   McFarlane, S. A., Marchand, R. T., and Ackerman, T. P.: Retrieval of cloud phase and crystal habit from Multiangle

1098   Imaging Spectroradiometer (MISR) and Moderate Resolution Imaging Spectroradiometer (MODIS) data, *J.*

1099   *Geophys. Res.-Atmos.*, 110, D14201, doi:10.1029/2004JD004831, 2005.

1100   Mei, L.L., Xue, Y., de Leeuw, G., von Hoyningen-Huene, W., Kokhanovsky, A.A., Istomina, L., Guang, J., Burrows,

1101   J. P.: Aerosol Optical depth retrieval in the Arctic region using MODIS over snow. *Remote Sensing of Environment*.

1102   128,234 -245, 2013a.

1103   Mei, L.L., Xue, Y., von Hoyningen-Huene, W., Istomina, L., Kokhanovsky, A.A., de Leeuw, G., Guang, J., Burrows,

1104   J. P.: Aerosol Optical depth retrieval over snow using AATSR data. *International Journal of Remote Sensing*. 34(14),

1105   5030 – 5041, 2013b.

1106 Mei, L. L., Rozanov, V., Vountas, M., Burrows, J., Levy, R., Lotz, W.: A Cloud masking algorithm for the XBAER

1107 aerosol retrieval using MERIS data. *Remote Sensing of Environment*. 197, 141-160,

1108 http://dx.doi.org/10.1016/j.rse.2016.11.016, 2017.

1109 Mei, L., Vandenbussche, S., Rozanov, V., Proestakis, E., Amiridis, V., Callewaert, S., Vountas, M., Burrows, J. P.,

1110 2020, On the retrieval of aerosol optical depth over cryosphere using passive remote sensing, *Remote Sensing of*

1111 *Enviroment*, 241, 111731, https://doi.org/10.1016/j.rse.2020.111731, 2020a.

1112 Mei, L.L., Rozanov, V., Ritter, C., Heinold, B., Jiao, Z.T., Vountas, M., Burrows, J.P.: Retrieval of aerosol optical

1113 thickness in the Arctic snow-covered regions using passive remote sensing: impact of aerosol typing and surface

1114 reflection model. *IEEE Transactions on Geoscience and Remote Sensing*. 10.1109/TGRS.2020.2972339, 1-15.

1115 2020b.

1116 Mei, L., Rozanov, V., Jäkel, E., Cheng, X., Vountas, M., and Burrows, J. P.: The retreival of snow properties from

1117 SLSTR/Sentinel-3 – part 2: results and validation, The Cryosphere Discuss. [preprint], https://doi.org/10.5194/tc-

1118 2020-270, in review, 2020c.Mishchenko MI, Travis LD, Lacis AA. Scattering, absorption, and emission of light by

1119 small particles. Cambridge University Press; 2002.

1120 Nakaya, U., Sekido, Y., General classification of snow crystals ad their frequency of occurrence. J. Fac. Sci.,

1121 Hokkaido Imperial Univ., Ser. II I-9, 234–264, 1938

1122 Nakaya, U.: Snow Crystals: Natural and Artificial, Harvard Univ. Press, Cambridge, 1954.

1123 Painter, T. H., Dozier, J., Roberts, D. A., Davis, R. E., and Greene, R. O.: Retrieval of subpixel snow-covered area

1124 and grain size from imaging spectrometer data, *Remote Sens. Environ.*, 85, 64– 77, 2003.

1125 Painter, T.H., Rittger, K., McKenzie, C., Slaughter, P., Davis, R.E., Dozier, J.: Retrieval of subpixel snow covered

1126 areas, grain size, and albedo from MODIS, *Remote Sensing of Environment*, 113, 868-879, 2009.

1127 Peltoniemi, J., Hakala, T., Suomalainen, J., & Puttonen, E.: Polarised bidirectional reflectance factor measurements

1128 from soil, stones, and snow. *Journal of Quantitative Spectroscopy and Radiative Transfer*, 110(17), 1940-1953,2009

1129 Platnick, S., Meyer, K. G., King, M. D., Wind, G., Amarasinghe, N., Marchant, B., Arnold, G. T., Zhang, Z.,

1130 Hubanks, P. A., Holz, R. E., Yang, P., Ridgway, W. L., and Riedi, J.: The MODIS Cloud Optical and Microphysical

1131 Products: Collection 6 Updates and Examples From Terra and Aqua, *IEEE Trans. Geosci. Remote*, 55, 502–525,

1132 2017

1133 Picard, G., Arnaud, L., Domine, F., and Fily, M.: Determining snow specific surface area from near-infrared

1134 reflectance measurements: Numerical study of the influence of grain shape. Cold Regions Science and Technology,

1135 56(1), 10–17. doi:10.1016/j.coldregions.2008.10.001, 2009.

1136 Pirazzini, R., Räisänen, P., Vihma, T., Johansson, M., and Tastula, E.-M.: Measurements and modelling of snow

1137 particle size and shortwave infrared albedo over a melting Antarctic ice sheet, *The Cryosphere*, 9, 2357-2381,

1138 https://doi.org/10.5194/tc-9-2357-2015, 2015.

1139 Pohl, C., Istomina, L., Tietsche, S., Jäkel, E., Stapf, J., Spreen, G., and Heygster, G.: Broadband albedo of Arctic

1140 sea ice from MERIS optical data, The Cryosphere, 14, 165–182, https://doi.org/10.5194/tc-14-165-2020, 2020a.

1141 Pohl C., Rozanov V.V. , Mei L. , Burrows J.P., Heygster G. and Spreen G.: Implementation of an ice crystal single-

1142 scattering property database in the radiative transfer model SCIATRAN, J. Quant. Spectrosc. Radiat. Transfer,

1143 doi: https://doi.org/10.1016/j.jqsrt.2020.107118,2020b

1144 Pope A., Gareth Rees, W., Fox, A.J. and Fleming, A.: Open access data in polar and cryo spehric remote sensing,

1145 *Remote sensing*, 6, 6183-6220, 2014.

1146 Qu, Y., Liang, S.L., Liu, Q., He, T., Liu, S.H. and Li ,X.W.: Mapping surface broadband albedo from satellite

1147 observations: A review of literatures on algorithms and products, *Remote sensing*, 7, 990-1020, 2015.

1148 Räisänen, P., Kokhanovsky, A., Guyot, G., Jourdan, O., and Nousiainen, T.: Parameterization of single-scattering

1149 properties of snow, *The Cryosphere*, 9, 1277–1301, https://doi.org/10.5194/tc-9-1277-2015, 2015.

1150 Räisänen, P., Makkonen, R., Kirkevåg, A., and Debernard, J. B.: Effects of snow grain shape on climate simulations:

1151 sensitivity   tests   with   the   Norwegian   Earth   System   Model,   *The   Cryosphere*,   11,   2919-2942,

1152 https://doi.org/10.5194/tc-11-2919-2017, 2017.

1153 Rozanov, V. V., Rozanov, A. V., Kokhanovsky, A. A., and Burrows, J. P.: Radiative transfer through terrestrial

1154 atmosphere and ocean: Software package SCIATRAN, *J. Quant. Spect. Rad. Trans.* 133, 13–71, doi:10.5194/acp-

1155 8-1963-2008, 2014.

1156 Saito, M., P. Yang, N. G. Loeb, and S. Kato: A novel parameterization of snow albedo based on a two-layer snow

1157 model with a mixture of grain habits, *J. Atmos. Sci.*, 76, 1419–1436, 2019.

1158 Satellite Snow Monitoring Community (SSMC), Perspectives for a European Satellite-based Snow Monitoring

1159 Strategy, White Paper, *Satellite Snow Monitoring Community*, ESA DUE GlobSnow-2 Consortium, 2014.

1160 Schneider, A., Flanner, M., De Roo, R., and Adolph, A.: Monitoring of snow surface near-infrared bidirectional

1161 reflectance factors with added light-absorbing particles, *The Cryosphere*, 13, 1753–1766, https://doi.org/10.5194/tc-

1162 13-1753-2019, 2019.

1163 Serreze, M. C. and Francis, J. A.: The Arctic amplification debate, *Climatic Change*, 76, 241–264, 2006.

1164 Sinnhuber, B.-M., Sheode, N., Sinnhuber, M., Chipperfield, M. P., Feng, W.:The contribution of anthropogenic

1165 bromine emissions to past stratospheric ozone trends: a modelling study. *Atmos. Chem. Phys.* 9, 2863-2871,

1166 https://doi.org/10.5194/acp-9-2863-2009, 2009.

1167 Stamnes, K., Li, W., Eide, H., Aoki, T., Hori,M. and Storvold, R.: ADEOSII/GLI snow/ice products - part I:

1168 Scientific basis, *Remote Sens. Environ.*, 111, 258–273, doi:10.1016/j.rse.2007.03.023, 2007.

1169 Taillandier, A. S., Domine, F., Simpson, W. R., Sturm, M., and Douglas, T. A.: Rate of decrease of the specific

1170 surface area of dry snow: Isothermal and temperature gradient conditions, J. Geophys. Res., 112, F03003,

1171 10.1029/2006jf000514, 2007.

1172 Tsukerman , E. and Veomett, E. : A Simple Proof of Cauchy's Surface Area Formula, *arXiv*, 1604.05815,2016

1173 Ulanowski, Z., Kaye, P. H., Hirst, E., Greenaway, R. S., Cotton, R. J., Hesse, E., and Collier, C. T.: Incidence of

1174 rough and irregular atmospheric ice particles from Small Ice Detector 3 measurements, *Atmos. Chem. Phys.*, 14,

1175 1649-1662, 10.5194/acp-14-1649-2014, 2014.

1176 Tomasi, C., Kokhanovsky, A. A., Lupi, A., Ritter, C., Smirnov, A., O'Neill, N. T., Stone, R. S., Holben, B. N., and

1177 Nyeki, S.: Aerosol remote sensing in polar regions, *Earth-Sci. Rev.*, 140, 108–157,

1178 doi:10.1016/j.earscirev.2014.11.001, 2015.

1179 Van de Hulst, H :Light Scattering by Small Particles, Dover Publications, 496 pages, 1981

1180   Warren, S. and Wiscombe, W.: A model for the spectral albedo of snow, II: Snow containing atmospheric aerosols,

1181   *J. Atmos. Sci.*, 37, 2734–2745, 1980.

1182   Wiebe, H., Heygster, G., Zege, E., Aoki, T., and Hori, M.: Snow grain size retrieval SGSP from optical satellite data:

1183   Validation with ground measurements and detection of snow fall events, *Remote Sens. Environ.*, 128, 11–20,

1184   https://doi.org/10.1016/j.rse.2012.09.007, 2013.

1185   Xiong, C., & Shi, J.: Snow specific surface area remote sensing retrieval using a microstructure based reflectance

1186   model. Remote Sensing of Environment, 204, 838–849. doi:10.1016/j.rse.2017.09.017,2018

1187   Yamaguchi, S., Ishizaka, M., Motoyoshi, H., Nakai, S., Vionnet, V., Aoki, T., Yamashita, K., Hashimoto, A., and

1188   Hachikubo, A.: Measurement of specific surface area of fresh solid precipitation particles in heavy snowfall regions

1189   of Japan, Cryosphere, 13, 2713-2732, 10.5194/tc-13-2713-2019, 2019.

1190   Yang, P., Bi, L., Baum, B. A., Liou, K.-N., Kattawar, G. W., Mishchenko, M. I. And Cole, B.: Spectrally consistent

1191   scattering, absorption, and polarization properties of atmospheric ice crystals at wavelengths from 0.2 to 100 μm, *J.*

1192   *Atmos. Sci.*.70, 330–347, 2013.

1193